國 立 交 通 大 學

電子物理系所

碩士論文

a軸取向正交結構鎦錳氧薄膜之磁性與電性研究

Magnetic and electric properties of the a-axis-oriented orthorhombic $LuMnO_3$ thin films

研 究 生：黃彥智

指導教授：莊振益 教授

中華民國九十九年七月

a軸取向正交結構鎦錳氧薄膜之磁性與電性研究

Magnetic and Electric Properties of the a-axis-oriented Orthorhombic $LuMnO_3$ Thin Films

研 究 生：黃彥智　　Student : Yan Jhih Huang

指導教授：莊振益 教授　　Advisor : Prof. Jenh-Yih Juang

國 立 交 通 大 學

電 子 物 理 系 所

碩 士 論 文

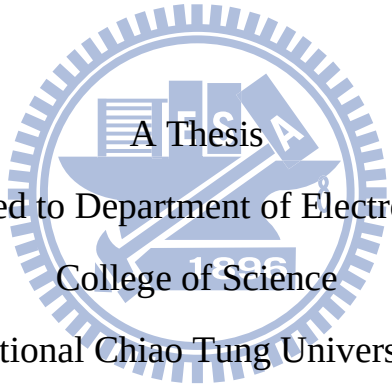

A Thesis

Submitted to Department of Electrophysics

College of Science

National Chiao Tung University

in partial Fulfillment of the Requirements

for the Degree of

Master

in

Electrophysics

July 2010

Hsinchu, Taiwan, Republic of China

中華民國九十九年七月

a軸取向正交結構鎘錳氧薄膜之磁性與電性研究

研究生：黃彥智　　指導教授：莊振益 教授

國立交通大學 電子物理系所碩士班

中文摘要

本研究使用脈衝雷射濺鍍系統在摻鈮鈦酸鍶(110)基板上成功製備出a軸垂直基板且軸向分離之正交結構鎘錳氧薄膜，並研究其磁性與電性。我們使用超導量子干涉儀量測磁化率與溫度變化關係，發現兩個磁性轉折點：第一個轉折點在a、b、c軸都有觀測到為尼爾溫度，約在43K，是由錳的反鐵磁磁序引起的；第二個轉折點只有發生在b軸約在30K，可能為錳的磁矩重新排列所導致的。電性測量發現a軸方向上相對電容率在30K附近有轉折，但是由極化對電場的曲線卻沒觀察到自發性極化，與理論預測之磁電關連性不同，推測可能是應變造成的影響。

Magnetic and Electric Properties of the a-axis-oriented Orthorhombic $LuMnO_3$ Thin Films

Student：Yan-Jhih Huang　　Advisor：Prof. Jenh-Yih Juang

Department of Electrophysics

National Chiao Tung University

Abstract

We have investigated the structure and magnetic properties of the a-axis-oriented orthorhombic $LuMnO_3$ (o-$LuMnO_3$) films deposited on Nb-doped $SrTiO_3$ (110) substrate by pulsed laser deposition. We observed the anisotropic properties in magnetic structure of o-$LuMnO_3$ by using SQUID (Superconductor Quantum Interference Device) to measure the temperature dependent susceptibility. Two distinctive magnetic transitions were observed for o-$LuMnO_3$ films. The first one locating around 43K was observed universally in each axis and presumably associated with the antiferromagnetic ordering of Mn moment. Consequently, it is assigned as the Neel temperature (T_N). The second transition was observed around 30K only when the field was

probed along the b-axis, which could be caused by Mn spin reordering. By electric measurement, a transition of the relative permittivity around 30K in a-axis was observed, but the spontaneous polarization was not seen in the electric field dependent polarization curves. It is different from the magnetoelectric correlation predicted by recent theories for these E-type multiferroic manganites. We suspect that the strain effect inherently existing in these epitaxial strain-stabilized orthorhombic films might have played a role.

Acknowledgement

The area of science is much wide and the deep investigations are needed. How to use limited time to search more and thorough knowledge must be guided by the professional professor. Thank my advisor Jenh-Yih Juang for his teaching and inspiring in these two years. Jiunn-Yuan Lin, Kaung-Hsiung Wu, Jin-Ming Chen, and Tzeng-Ming Uen also give me many ideas about physics.

When I encountered difficulties, I got much assistance from partners, Bo-Cyuan Lai, Chun-Yang Chang, Wei-tsung Tang, Bi-Hsuan Lin, Kai-Ting Chang, Chang-Yu Yang, Tsung-Yu Tsai, Chih-Chang Hsieh, Yao-Tsung Chen, Jia-Bin Wang, Jun-Yu Lin, Chia-Wei Wu, Pei-Ru Lee, Chia-Chih Hsu, Chung-Chen Chien, Yu-Jen Chen, Yu-Ting Liu, and Tjung-Han Lin.

I am grateful to Sunsly Slowry, Icey, Linya, and Chia-Chia Wu for secrets.

Table of Contents

List of Tables

List of Figures

Chapter 1 Introduction

1.1 Background

Materials with magnetism and ferroelectricity coexist simultaneously are called multiferroics [1]. It is very interesting that magnetoelectric effect was revealed in some multiferroic materials, because it implies that the electric properties can be controlled by applied magnetic field and vice versa [2~4].

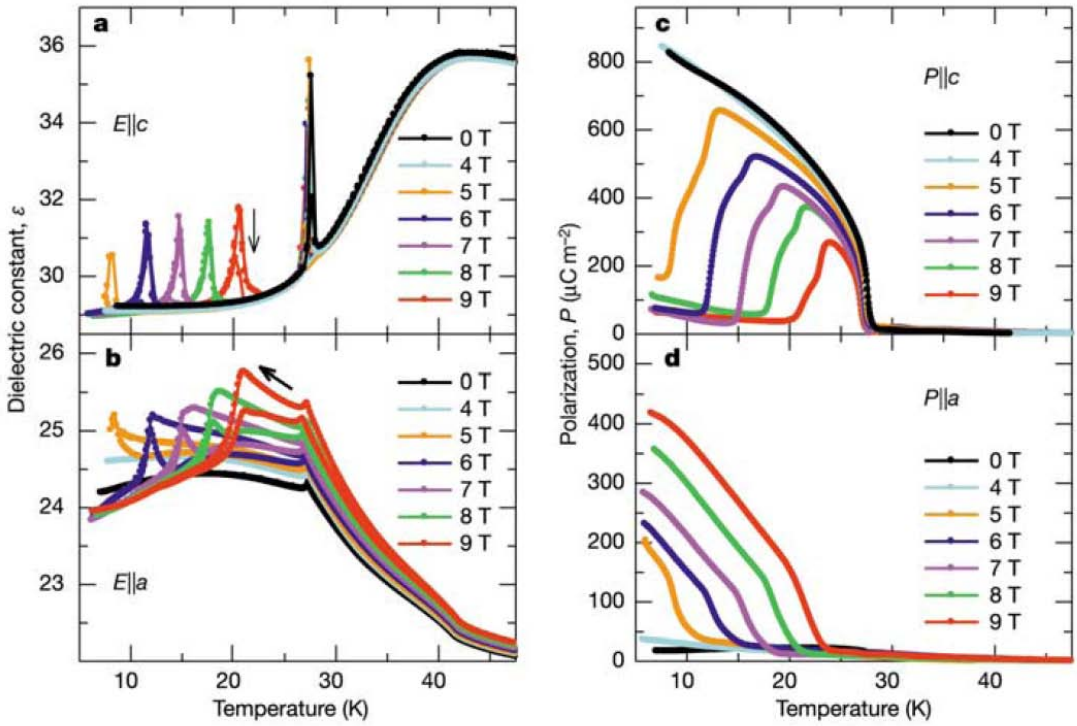

Fig. 1.1 Electric polarization flop induced by magnetic fields in $TbMnO_3$. a–d, temperature profiles of dielectric constant at 10 kHz (a and b) and of electric polarization along the c- and a-axes (c and d), respectively, at various magnetic fields in single crystals of $TbMnO_3$. Magnetic fields are applied along the b-axis [2].

T. kimura et al. [2] has reported the magnetic control of ferroelectric polarization of $TbMnO_3$. Figure 1.1 (a) and (b) shows no distinct change of ε for either direction was observed at temperatures above T_{lock}(~27K). Although the sharp peak at T_{lock} in ε_c is not sensitive to the application of magnetic fields, another peak feature at $T_{flop}(B)$ shows up in ε_c below T_{lock} above 5 T. The magnetic field- induced sharp maximum is shifted towards higher temperature with increasing magnetic field from $T_{flop}(5\ T) \approx 8K$ to $T_{flop}(9\ T) \approx 20\ K$. The component ε_a also shows a remarkable magnetic field effect. By applying magnetic fields above 5 T, ε_a exhibits an extra peak structure at T_{flop}, which is again dependent on the strength of the applied field. Measurements of P in magnetic fields have revealed the origin of the magnetic-field-induced anomaly in ε. In Fig. 1.1 (c), by applying a magnetic field above 5 T, the spontaneous polarization in P_c is considerably suppressed below T_{flop}. With increasing magnetic field, the temperature region with finite P_c shrinks, corresponding to the shift of T_{flop}. By contrast, the application of a magnetic field induces a finite P_a (Fig. 1.1 (d)). The onset temperature of a finite P_a coincides well with T_{flop}, and increases in accord with the increase of T_{flop} by applying a magnetic field. These results show that the spontaneous polarization is switched (‘flopped’) from the direction along the c-axis to the direction along the a-axis at T_{flop}, and the strong magnetic field dependence of T_{flop} causes the notable magnetic field effect on ε and P.

Some predictions about the magnetism induced polarization in E-phase $RMnO_3$ were reported subsequently [5~9]. The estimation of magnetism-induced polarization is about 0.5~12μC/cm^2 along the a-axis and is much bigger than that of the spiral-phase $RMnO_3$ (ex. $TbMnO_3$). Even though the single crystal of the E-phase $RMnO_3$ have not been successfully prepared, the polarization of the polycrystalline E-phase $RMnO_3$ prepared by high-temperature high-pressure processes was investigated [10]. A direct comparison of the spontaneous polarization along the specific crystallographic orientation with the theoretical prediction, however, still remains to be realized.

1.2 Motivation

According to the prediction mentioned above, large probability of the magnetic-induced polarization in the a-axis indicates that it is possible to confirm the theoretical prediction by using the well-developed skills of epitaxial strain-stabilized crystalline structures of materials commonly practiced in PLD process. The primary motivation of this study is to search for the anisotropic magnetism and the electric properties along the a-axis-orientation of the orthorhombic $LuMnO_3$ stabilized by the strain of Nb-doped $SrTiO_3$ (110) substrates.

Chapter 2

Basic physical properties of E-phase $RMnO_3$ manganites

In order to investigate the magnetic and electric properties of o-$LuMnO_3$, it is essential to explore the fundamental basis of magnetic behaviors in these manganites. In the o-$LuMnO_3$, the superexchange causes antiferromagnetism between spins of Mn ions, while the double exchange mechanism can lead to electron hopping between Mn ions and producing ferromagnetism. The polarization induced by magnetism that is predicted to be intimately related to the details of these two interactions by theoretic calculations [5].

2.1 Superexchange

The superexchange is described as the indirect interaction caused by the virtual hopping of electrons between the oxygen ions and neighboring metal ions. Fig. 2.1 illustrates schematically the superexchange interaction that takes place along the Mn-O-Mn chain of the MnO_6 octahedron crystal structure [14]. The overlap of the wave functions of the p- and d-orbitals leads to the p-d rehybridization. The electrons at the left-hand-side of the oxygen p-orbital could mediate to the neighboring manganese. Due to the Pauli's exclusion principle, the electrons in manganese must be antiparallel to the mediating one. The remaining electron in the oxygen p-orbital

can be paired with the other neighboring manganese. Therefore, these two neighboring manganese ions are effectively coupled by the bridging of oxygen ion and form antiferromagnetic ordering.

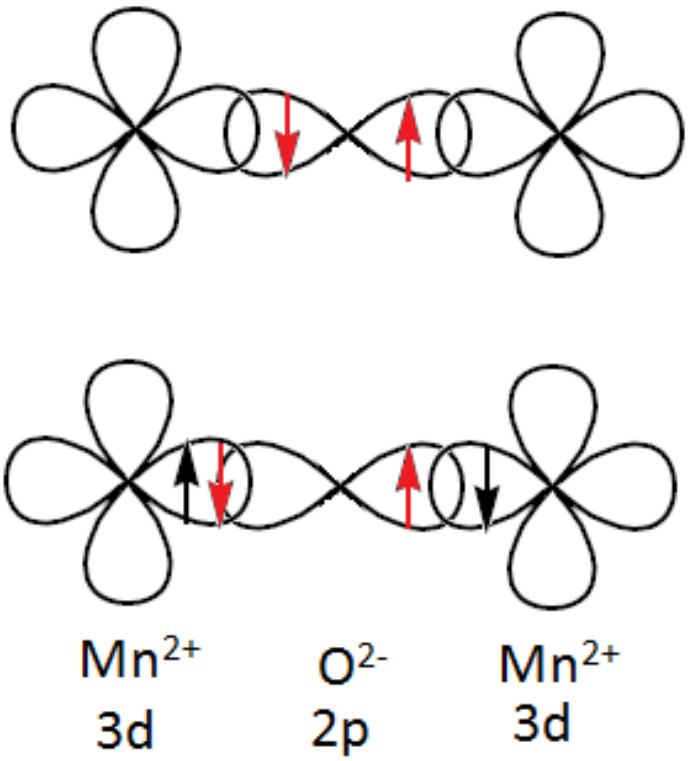

Fig2.1 Top: The wave function of O^{2-} 2p and Mn^{3+} 3d orbital overlapping Bottom: antiferromagnetic ordering is due to the superexchange interaction (reproduced from reference [13]).

2.2 Double exchange

Double-exchange, originally proposed by Clarence Zener [15], explains how electrons exchange between two species and why materials become ferromagnetic.

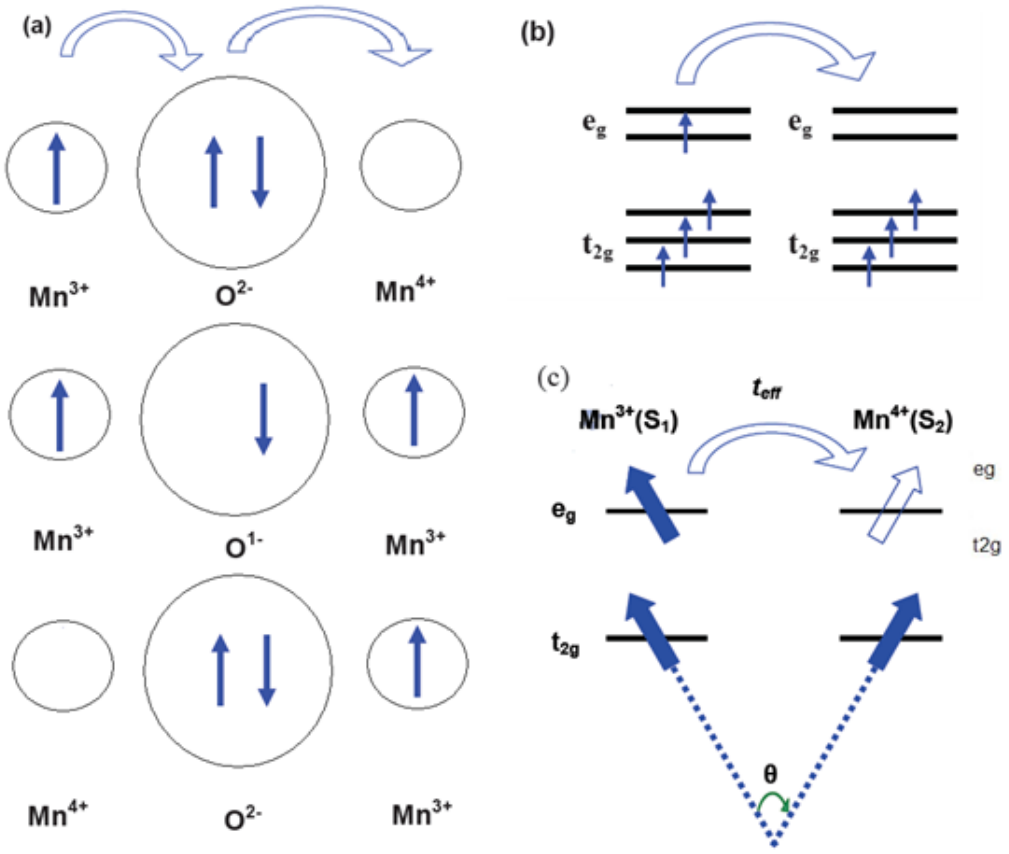

Fig2.2 (a)(b)The hopping process of the double exchange (c)effective hopping between the two noncollinear spins (reproduced with reference [13]).

Take the electrons hopping among Mn^{3+}-O^{2-}-Mn^{4+} as an example. The degeneracy of the d states of the transition metal manganese is lifted and splits into a

doublet (e_g) and triplet (t_{2g}) degenerate states by crystal field. As a result, the Mn^{3+} and Mn^{4+} ions will have the ground state configuration of $t_{2g}^3 e_g^1$ and $t_{2g}^3 e_g^0$, as illustrated schematically in Fig. 2.2(b). The hopping process is illustrated in Fig. 2.2(a). Furthermore, according to the Hund's rule and the Pauli exclusion principle, the magnetic moments of these hopping electrons must be parallel to each other, causing the ferromagnetic state in the two manganese ions. In Fig.2.2(c), the effective hopping between two neighboring transition metal ions is defined as $t_{eff}=t*\cos(\theta/2)$ where θ was the angle between the two spin orientations [16]. For the antiparallel spin situation, $\theta=180^o$ (antiferromagnetic), the effective hopping will be zero and electrons cannot hop in this situation. In contrast, hopping will be the largest when $\theta=0^o$

2.3 Crystal field and Jahn-Teller effect

The electrostatic field arising from the surrounding ions influences the localized electrons in d or f states was called crystal field. We focus on the effect of octahedral crystal fields on manganese oxide (MnO_6). The respective electronic distribution of the d-orbitals is schematically illustrated in Fig.2.3 [17]. The Mn ion locates at the center of the MnO_6 octahedron and is surrounded by six oxygen anions. The five fold degeneracy of the d-orbitals is lifted and splits into $e_g(d_{x^2-y^2}$ and $d_{3z^2-r^2})$ and $t_{2g}(d_{xy}$,

d_{yz} and d_{zx}) orbitals caused by the inhomogeneous electrostatic field originated from the neighboring ions (see Fig.2.4(a)). The e_g orbitals point directly towards the charges of the ligands, and so they have a greater electrostatic repulsion. The t_{2g} orbitals have lobes which point toward the direction between the charges, so the electrostatic repulsion is weaker. The energy splitting between the e_g and t_{2g} states has been usually set to be 10Dq. Due to the energy conservation law, the energy of the e_g orbital is raised up by 6Dq and that of the t_{2g} orbital is lowered by 4Dq [18].

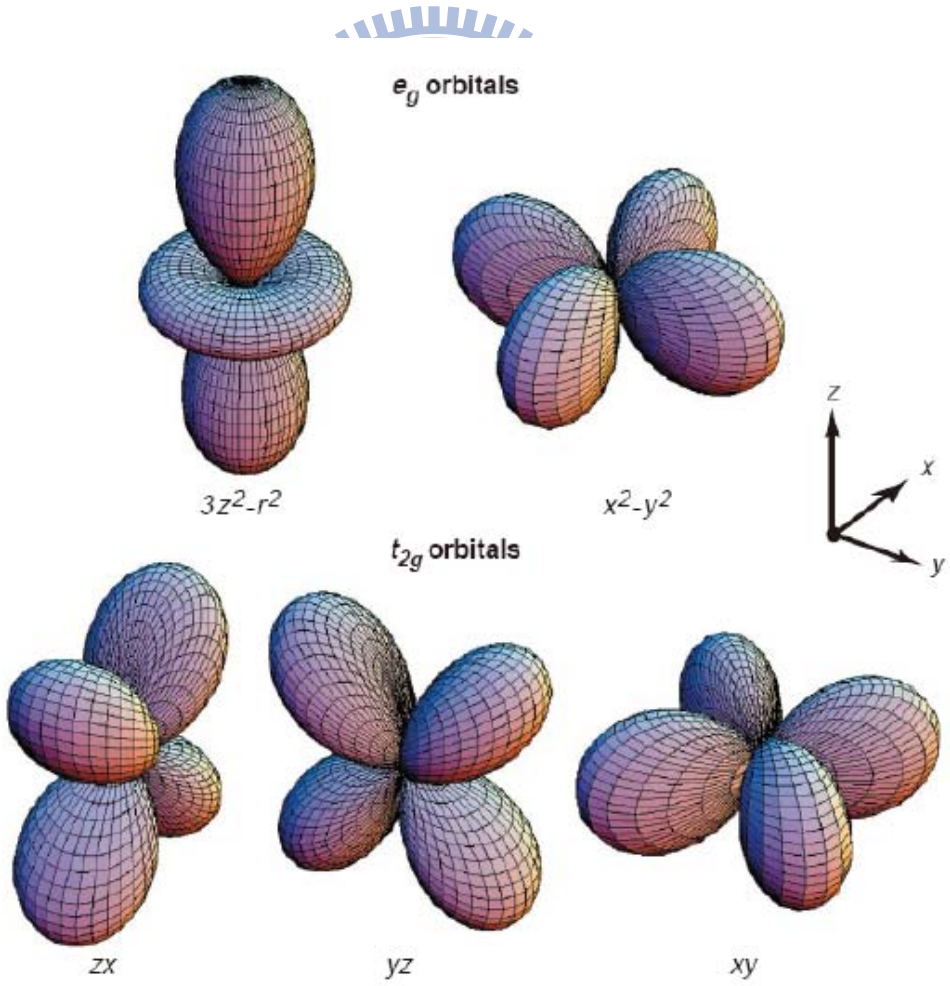

Fig.2.3 The electronic distribution of five d orbitals [17].

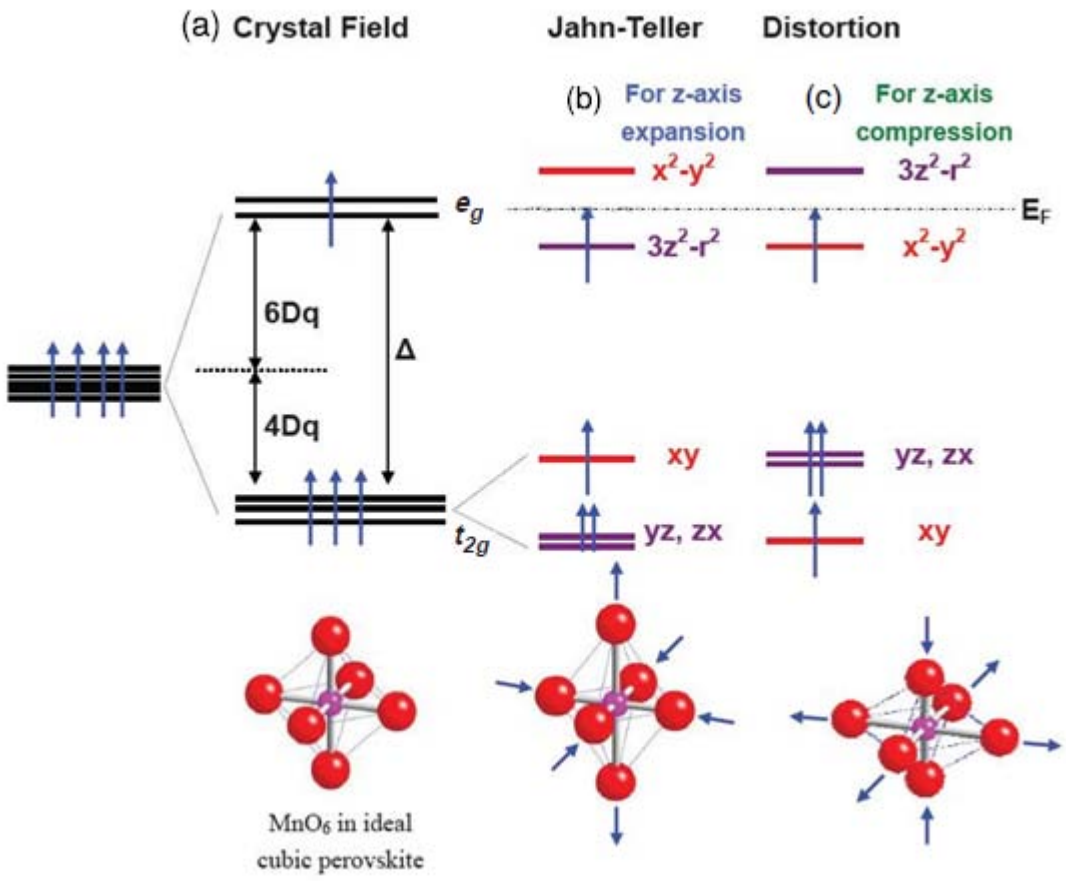

Fig. 2.4 Illustration of the energy level splitting (a)by crystal field and (b) and (c) Jahn-Teller distortion. Pink and red ball denote the Mn and O ions, respectively (reproduced from reference [13]).

For highly symmetrical molecules, there always exists at least one non-totally symmetric vibration that makes electronically degenerate states unstable [19]. In order to lower the energy, the crystal would be distorted and the degeneracy would be broken. Energy splitting is induced by the distortion of MnO_6 and such a spontaneous displacement is the so-called Jahn-Teller effect. Fig. 2.4(b) and (c) shows two distortion modes of the MnO_6 octahedrons. For z-axis expansion mode (Fig. 2.4(b)), the repulsion between the electron in $d_{3z^2-r^2}$ orbital and the ligand decreases, the

energy of $d_{3z^2-r^2}$ orbital is lower. The energy of $d_{x^2-y^2}$ orbitals is raised by the shortened ligands along the x- and y-axis. Thus, the degeneracy of e_g orbitals would split. The d_{xy}, similar to $d_{x^2-y^2}$, is repelled by the closer ligands on the x- and y-axis, whereas d_{yz} and d_{xz}, similar to $d_{3z^2-r^2}$, are lowered in energy due to weaker repulsion.

2.4 Crystal structure of the manganites ($RMnO_3$)

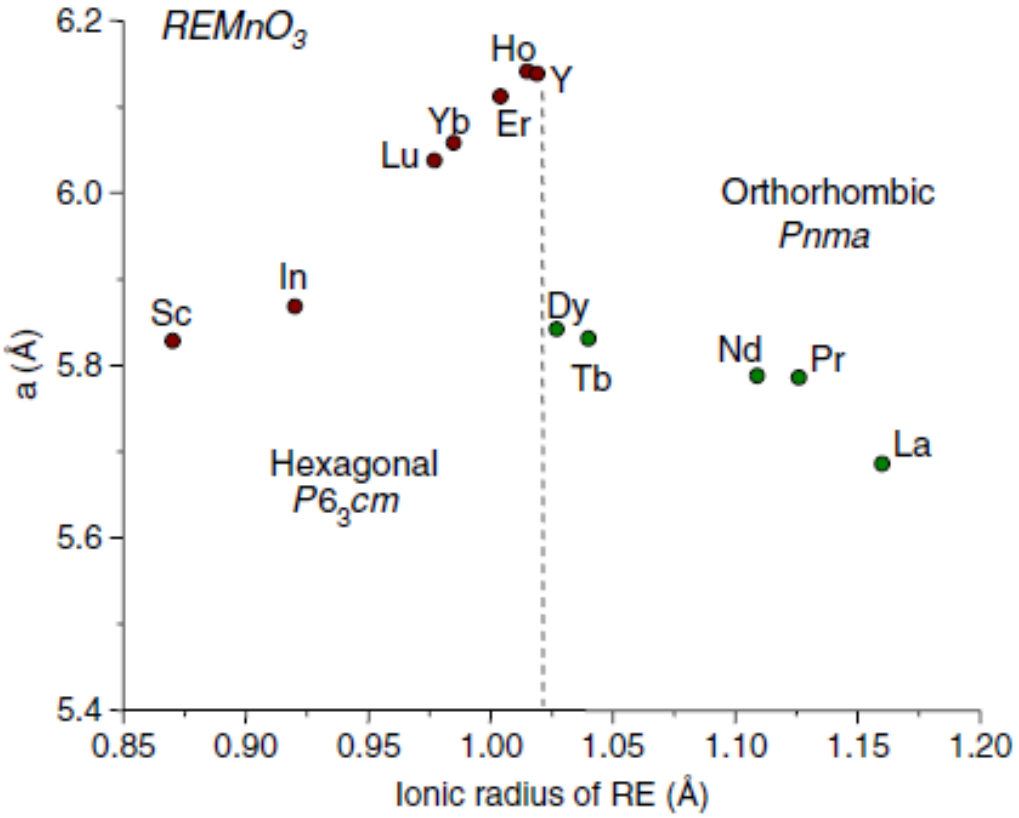

Fig.2.5 Evolution of the lattice structure in $REMnO_3$ as a function of the size of the rare earth [20].

The $RMnO_3$ with larger rare earths, R=La-Dy, have stable orthorhombic structure in Pnma space group, whereas the $RMnO_3$ with smaller rare earths, R=Sc, Y

and Ho-Lu, have stable hexagonal structure in $P6_3cm$ space group (see Fig. 2.5). Nevertheless, we have prepared the orthorhombic perovskite with smaller rare earths in form of thin film by stabilizing the structure with the epitaxial strain between the substrate and film.

Orthorhombic $RMnO_3$ belongs to perovskite-structure oxide, ABO_3, which is illustrated in Fig. 2.6. Where A and B are R and Mn, respectively. Mn resides at the center of the octahedron which is surrounded by six oxygen, and R locates at the corner of the unit cell.

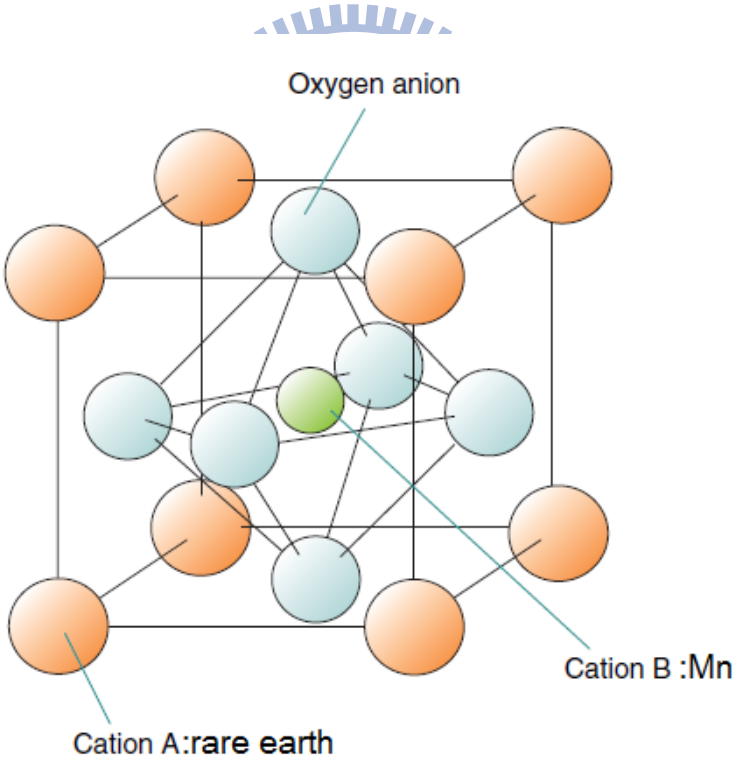

Fig.2.6 The perovskite structure (reproduced from[21]).

We use Pbnm space group to describe the orthorhombic $RMnO_3$, but another space group setting Pnma is also frequently used. These two space groups can be

easily converted to each other as displayed in Table 2.1.

Example: $LuMnO_3$

$LuMnO_3$ lattice constant(Å)	**Pbnm**	**Pnma**
5.20	**a-axis**	**c-axis**
5.79	**b-axis**	**a-axis**
7.30	**c-axis**	**b-axis**

Table 2.1 The relation of Pbnm and Pnma space group [7][22].

2.5 Models for magnetic structure of orthorhombic $RMnO_3$

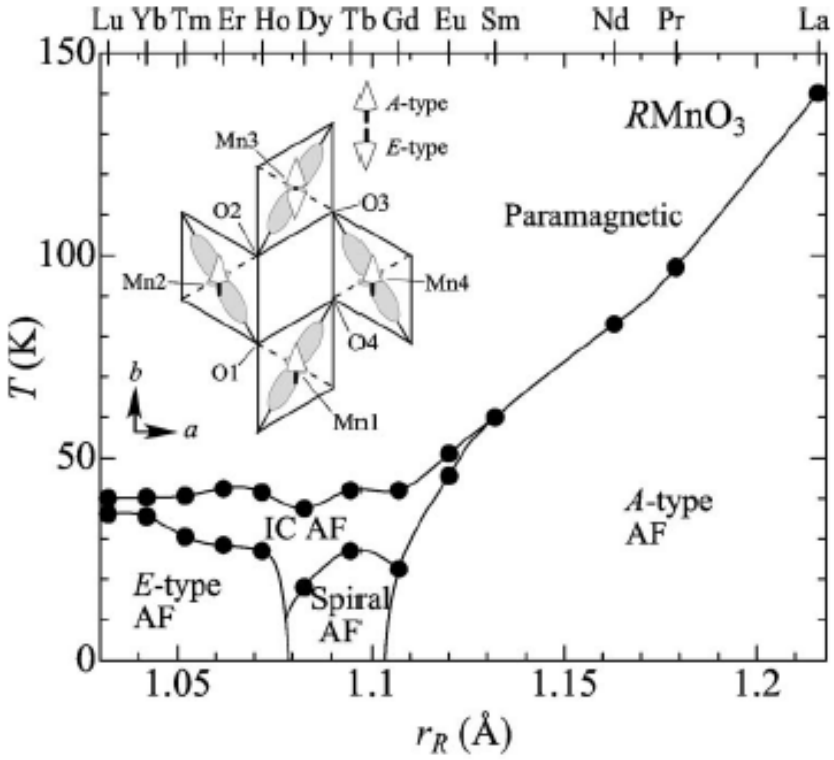

Fig. 2.7 The phase diagram of orthorhombic $RMnO_3$ [23].

The magnetic structure of orthorhombic $RMnO_3$ evolves with the ion size of rare earth elements according to the phase diagram reported by Tachibana et al. [23] (as shown in Fig. 2.7). For R=La-Sm, the magnetic structure is A-type antiferromagnetic order below the Neel temperature. For R=Eu and Gd, a sinusoidal incommensurate (IC) structure precedes A-type structure on cooling. Moreover, the A-type AF structure is no longer the stable ground-state structure when the ion size of rare earth gets smaller. The IC structure transforms to a spiral structure for R=Tb and Dy, while it locks to the E-type AF structure for R=Ho-Lu.

The A-type magnetic structure

In the A-type AFM ordering, the spins exhibit ferromagnetic order within the ab plane while the interplanar coupling is antiferromagnetic, are depicted in Fig. 2.8

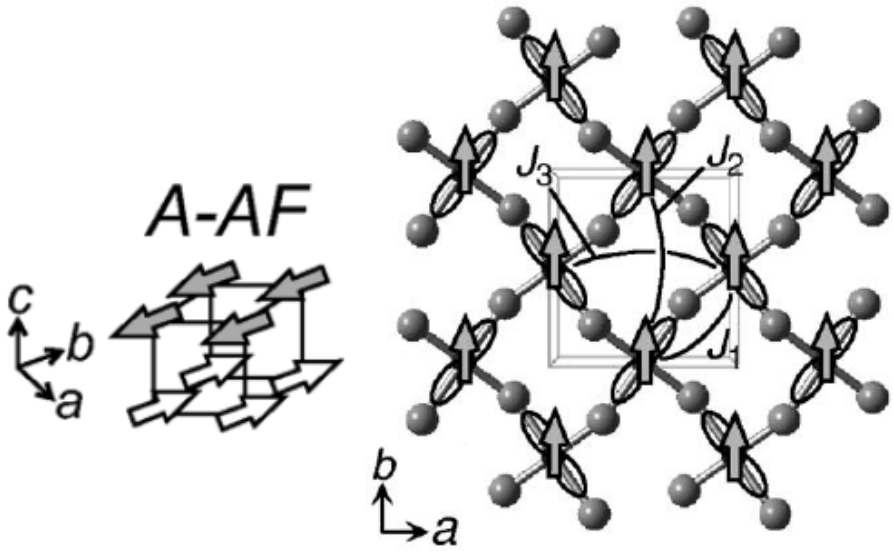

Fig. 2.8 A-type magnetic structure [24][25], the arrows indicate the spins of Mn^{3+}.

The spiral magnetic structure

For instance, the spiral magnetic structure in $TbMnO_3$ has spin rotate in the bc plane as temperature below T_{lock}, are shown in Fig. 2.9 (a). This type of magnetic structure will induced a spontaneous electric polarization as a result of spin-orbital interactions (see Fig. 2.9 (b)).

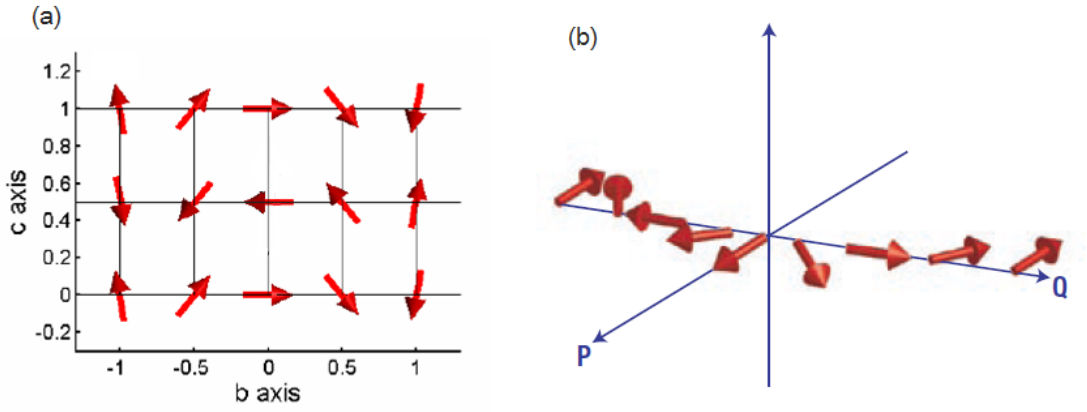

Fig. 2.9 (a) The spiral magnetic structure with spins rotating in the (b, c)-plane [26] (b) Polarization (P) lies in the plane of the spiral, but perpendicular to its propagation vector Q [27].

The E-type magnetic structure

In E-type magnetic structure, the spins were aligned in b-axis. The magnetic ordering is ferromagnetic in a-axis, and it is antiferromagnetic in b-axis. The interplanar coupling is antiferromagnetic coupling (shown as Fig. 2.10).

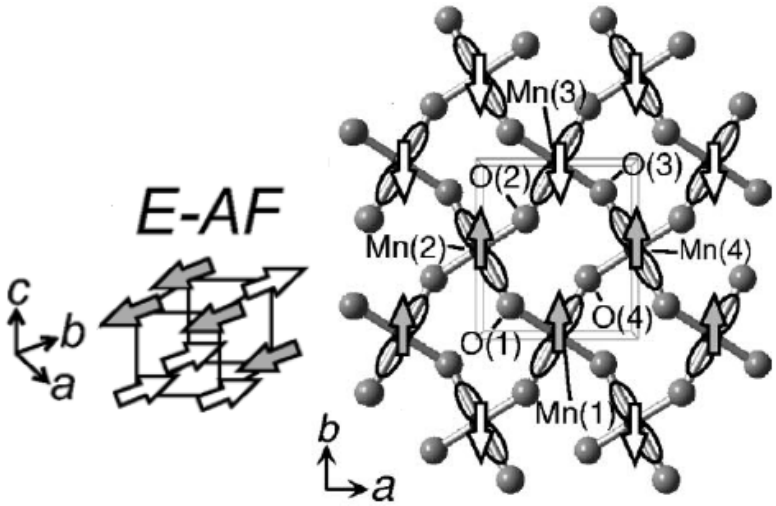

Fig. 2.10 E-type magnetic structure [24][25], the arrows indicate the spins of Mn^{3+}.

2.6 Magnetically induced polarization of E-phase $RMnO_3$

Sergienko et al. [5] by considering mechanisms other than spin-orbit interaction have estimated the polarization of the E-type $RMnO_3$ can reach to about 0.5~12 $\mu C/cm^2$, which is more than "2" orders of magnitude enhancement over that of the spiral phase $RMnO_3$. The polarization in this case is induced along the a-axis in Pbnm space group setting. As depicted in Fig. 2.11, the ferromagnetic zigzag chain has double exchange behavior, so the bond angle φ_0 will tend to 180^o in order to lower the hopping energy. At the same time, the lattice elastic energy increases with bond angle. As a result of the competition, the bond angle reaches an optimal angle φ ($\varphi_0<\varphi<180^o$) that results in the displacement of oxygen anion causing the polarization in a-axis.

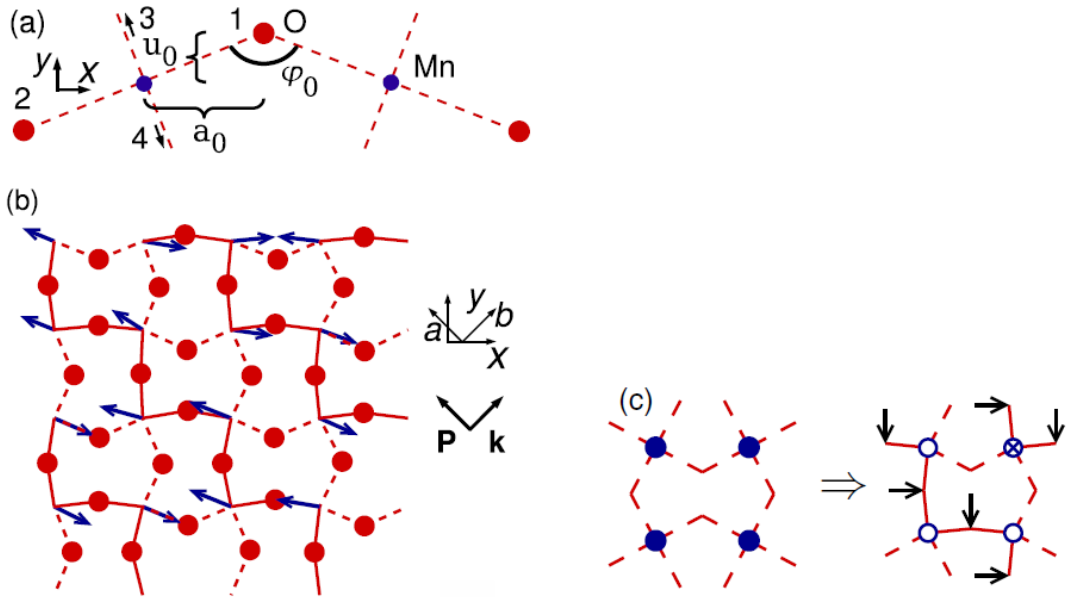

Fig. 2.11 (a) The starting configuration of a Mn-O-Mn bond. Numbers 1–4 enumerate the O atoms surrounding one Mn. (b) The ferromagnetic zigzag chain links are shown as solid lines. The displacements of the oxygen atoms are exaggerated. (c) Left: The local arrangement of the Mn-O bonds with disordered Mn spins (full circles). Right: Oxygen displacements (arrows) within the chains of opposite Mn spins (open and crossed circles) in the E-phase [5].

Chapter 3 Experiment

3.1 Sample preparation

3.1.1 Target fabrication

We prepared the hexagonal phase $LuMnO_3$ by solid-state reaction methods as the target to be used for pulsed laser deposition.

Procedures for preparing the hexagonal $LuMnO_3$ bulk are described below:

1. Mix the $MnCO_3$(99.95%), Lu_2O_3(99.99%) with the proper proportion.

2. Heat the mixture at 1200℃ for 24 hours to facilitate reactions among the constituents.

3. Grind the mixture to ensure the well mixing.

4. Press the mixture and then sinter it at 1200℃ for 24 hours.

5. Repeat steps 3 & 4 for three times.

To promote the crystalline quality of the sintered pellet, the increment of heating and cooling was kept at 5℃ per minute during the process.

The target used in this study was prepared by Tsai and the details of the target preparation and characterization were described previously [12].

3.1.2 Pulsed Laser Deposition (PLD)

In PLD process, a high energy laser pulse is focused on the surface of a solid target. After absorbing the strong electromagnetic radiation, local area of the solid

target is instantaneously vaporized to form a plume which would be deposited on the chosen substrate. By the strain caused by the slight lattice mismatch between the film and the substrate, the structure of $LuMnO_3$ transforms from hexagonal to orthorhombic during deposition. To prepare the a-axis thin film, we have tried different deposition conditions. The films were grown by 248nm KrF excimer laser with laser energy density modulating from 2 to 4 J/cm^2, repetition rate varying from 5 Hz to 10 Hz, the temperature of substrate changing from 800℃ to 880℃, and oxygen partial pressure ranging between 0.05 torr to 0.2 torr.

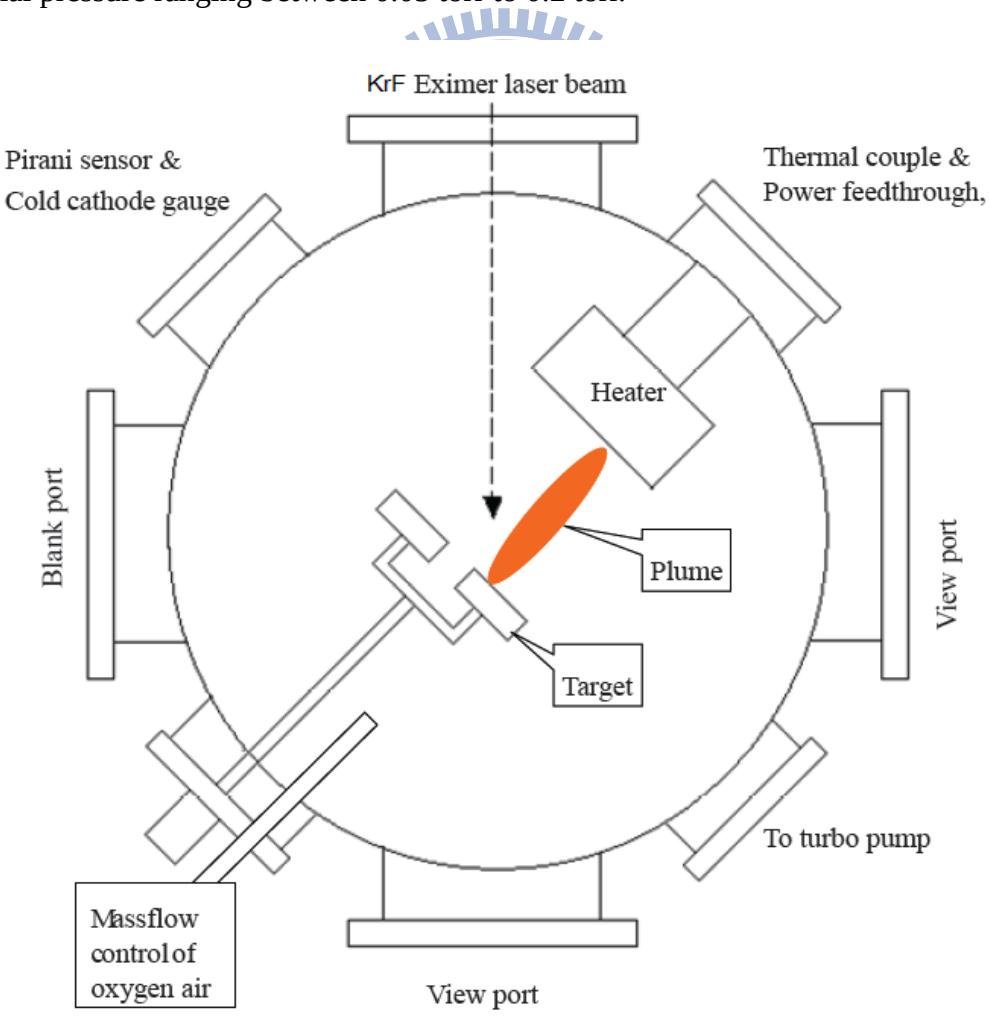

Fig. 3.1 Schematics illustrating the configuration of the pulsed laser deposition system [13].

Procedures for preparing the o-$LuMnO_3$ film are described below：

1. Clean the substrate in acetone, methanol, and DI water under ultrasonic vibration for 5 minutes, respectively.

2. Dry and clean the surface of substrate by blowing nitrogen gas.

3. Attach the substrate on the stainless steel plate by silver paste.

4. Heat the plate at 150℃ to remove the solvent till the silver paste is solidified.

5. Put the plate in chamber of PLD system with thermal couple imbedded.

6. Pump the chamber till the base pressure is lower than 10^{-7} torr for 1hour at least.

7. Heat the substrate to the preset temperature.

8. Set the power and repetition rate of excimer pulsed laser.

9. Start the excimer laser and aerate the chamber with oxygen to the expected pressure at the same time.

10. When deposit the film on the substrate, watch the partial pressure and the situation of the excimer laser.

11. Quench the substrate to room temperature after completing the deposition by filling the chamber with O_2 (1 atm).

12. Take out the sample.

3.2 Characterization of thin film

3.2.1 X-ray diffraction

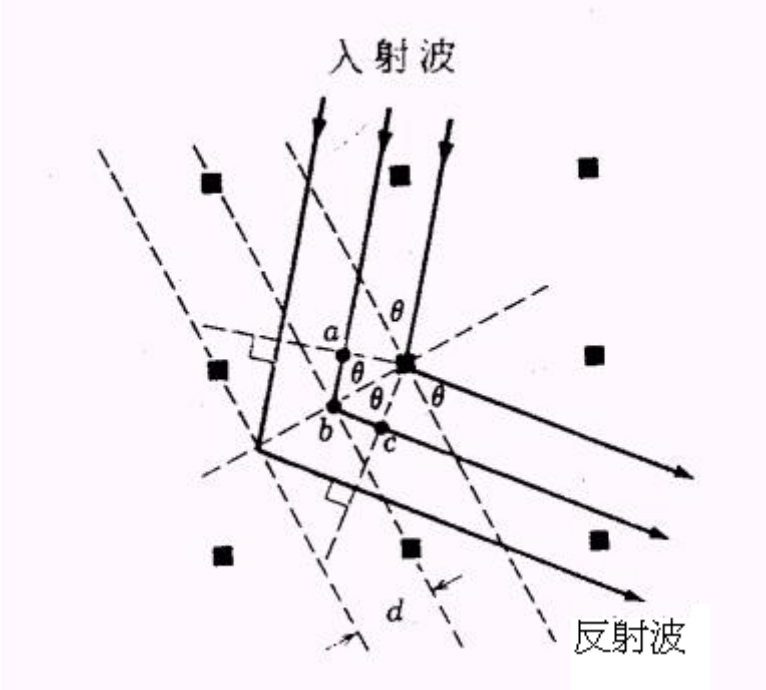

Fig 3.2 The schematic illustration of the XRD process.

We used X-ray diffraction (XRD) measurement to analyze the crystal structure of $LuMnO_3$. The diffraction pattern of XRD is described by the Bragg's law;

$$2d \sin\theta = n\lambda$$

Where d is the distance between successive parallel planes along certain crystallographic orientation, θ is the angle between the incident X-ray and the lattice plane, n is an integer, and λ is the wavelength of the X-ray. XRD can also be used as a tool for the preliminary analysis of composition. The simple schematic illustration of the diffraction conditions described by the Bragg's law is shown in Fig.3.2.

3.2.2 Alpha step profilometer

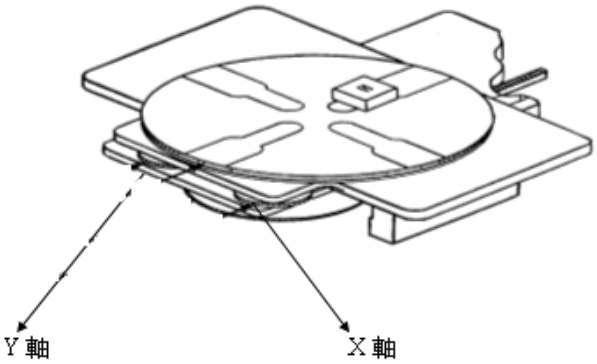

Fig 3.3 The configuration of α step profilometer.

We used α-step profilometer to probe the surface profile of a sample and to measure the thickness of thin film. This instrument consists of a stylus that is dragged across the surface while maintaining a constant vertical contact force. The stylus thus follows the topography of the sample, and the height profile is recorded. According to the height profile, the thickness and roughness are assessed.

3.2.3 X-ray reflectometry

X-ray reflectometry (XRR) is a technique for precise measurement of the thickness of a thin layer. When impinged on a sample below the critical incidence angle, which is related to the material of the film, XRR exhibits total external reflection. In contrast, as the angle of reflection is increased to exceed the critical angle, X-ray penetration occurs and the X-ray reflected from the buried interface

interfere with surface reflected radiation to give rise to interference fringes. Therefore, the thickness and interfacial roughness of the sample could be measured. Because this technique does not rely upon material crystallinity, it can be used to characterize amorphous as well as crystalline layer. In this study, we obtain the thickness of thin film by the periodicity of the obtained Kiessig fringe with $T \approx \frac{2\pi}{\Delta q}$, where T is the thickness and Δq is periodicity of Kiessig fringe.

3.2.4 Four-circle diffractometer

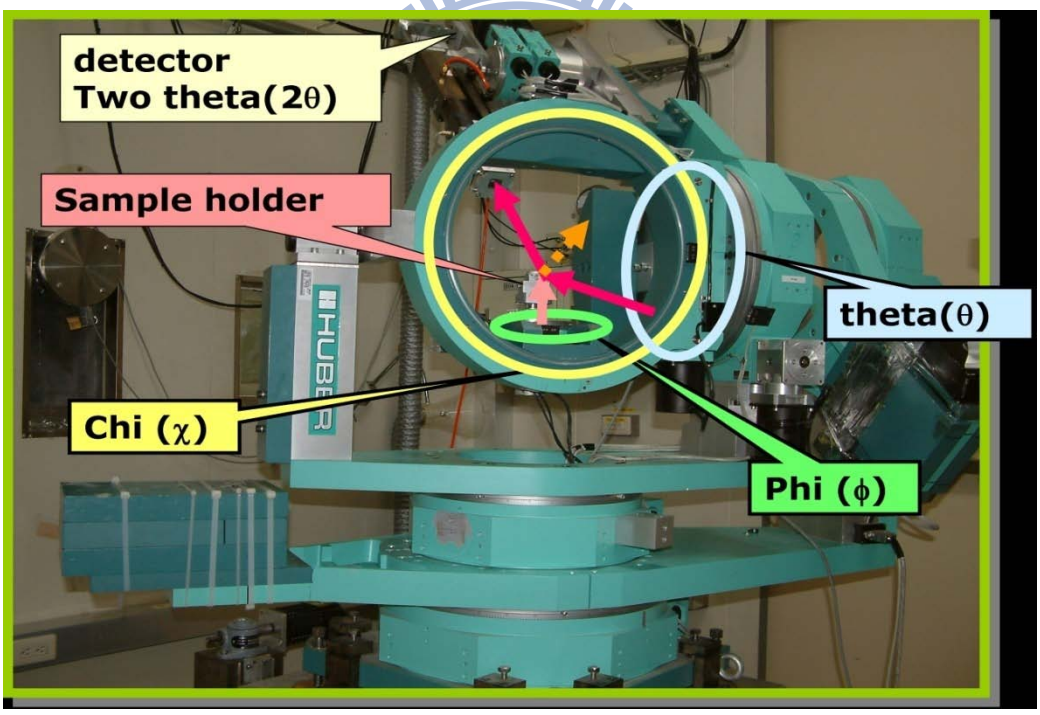

Fig. 3.4 Four-circle diffractometer [12].

Four-circle diffractometer, where the four circles are θ, χ, Φ, and 2θ was used to determine the texture, lattice parameters, the thickness of thin films and epitaxial relationship between film and substrate. It is an instrument frequently used in X-ray

crystallography to determine the shape and symmetry of the unit cell of the film. Placing in the goniometer head with an arbitrary orientation, the film is illuminated and rotated to measure the intensity of the diffracted radiation as a function of beam and sample orientation. If the dimensions of the unit cell were known, they can be used to calculate the settings of the four angles needed to observe a specific orientation. It can help us do X-ray diffraction (XRD), Φ-scan and X-ray reflectometry (XRR) measurements. The instrument was provided by National Synchrotron Radiation Research Center (NSRRC).

3.2.5 Superconducting quantum interference device

Superconducting quantum interference device (SQUID) is a delicate equipment integrating electronic, mechanical, low-temperature, and vacuum techniques for measuring magnetization with high sensitivity and precision, based on superconducting loops containing Josephson junctions. SQUID combines two Josephson junctions connecting in parallel used to measure extremely weak magnetic signals and its sensitivity is about 10^{-8} emu with 0.1T external magnetic field applied. The Josephson junction often consists of a tunnel barrier sandwiched by two superconducting electrodes. A much more sensitive direct current (DC) SQUID consists of two parallel Josephson junctions in a loop of inductance L so that electrons

tunneling through the junctions demonstrate quantum interference, dependent on the strength of the external magnetic field within a loop. Since demonstrating resistance in response to even slight variations in a magnetic field, DC SQUID is presently the most sensitive magnetometer available.

Fig. 3.5 Superconducting Quantum Interference Device.

3.2.6 Cryogenic refrigeration system

In order to control the temperature of the measurement, we use the cryogenic refrigeration system, as shown in Fig. 3.6. The sample was set on the stage of the expander module which was pumped with the pumping station and was cooled by the water-cooled compressor module. The LTC-11 temperature controller can provide heat to the stage of expander module by applying the current to the heater inside, so we can minitor the temperature in a rather wide range. The temperature range is about 11 K to 300 K.

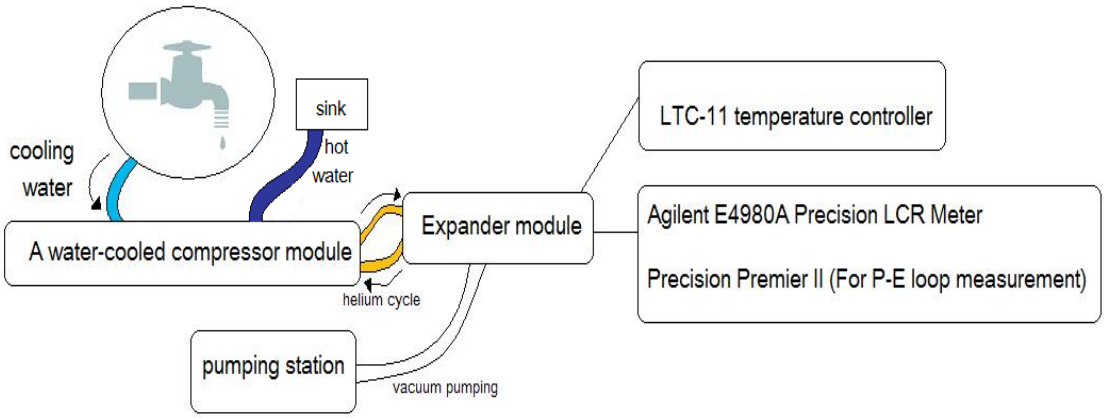

Fig. 3.6 Cryogenic refrigeration system.

3.2.7 Polarization-Electric field curves

We used the precision premier II ferroelectric test system to measure the polarization-electric field curves (P-E curves) of the thin film. The charge measurement circuit has an input current amplifier followed by a hardware integrator. The output of the integrator is a voltage that directly represents the total charge (not

current) exchanged between the test circuit and the sample at each measurement point in the test. On the Hysteresis test, the polarization values are the output voltages of the integrator multiplied by the current amplifier ratio and the sense capacitor, both are linear constants.

The maximum voltage of this instrument is 100 V and the voltage resolution is 76μV. The hysteresis frequency range can be varied from 0.033 Hz to 100 kHz.

3.2.8 Capacitance-Temperature curves

We used Agilent E4980a LCR meter to measure capacitance-temperature curves(C-T). The Agilent E4980A is a general-purpose LCR meter for incoming inspection of components, quality control, and laboratory use. The E4980A is used for evaluating LCR components, materials, and semiconductor devices over a wide range of frequencies (20 Hz to 20 MHz) and test signal levels (0.1 mV to 2 V, 50 μA to 20 mA (rms)). The sensitivity on measuring capacitance is about 10^{-12}F.

The relation between capacitance and relative permittivity is

$$C = \varepsilon_r \varepsilon_0 \frac{A}{d}$$

C is capacitance, ε_r is relative permittivity, ε_0 is vacuum permittivity, A is area of the pattern, and d is the thickness of o-$LuMnO_3$ thin film.

3.2.9 How to make electrodes connection

We used the Nb-doped $SrTiO_3$ (NSTO) as the bottom electrode and the top electrode is the gold thin film patterned on o-$LuMnO_3$ thin film. In Fig. 3.7 (a), the top drawing shows the side view and the bottom drawing shows the top view of the electrode configuration, respectively. Fig. 3.7 (a) to (c) demonstrate the processes of how we connected the copper wires to the electrodes. Fig. 3.7 (a) the gold thin film was patterned, (b) the small pieces of o-$LuMnO_3$ film and substrate in the corner was scraped, and (c) copper wires were attached onto the electrodes with silver paste.

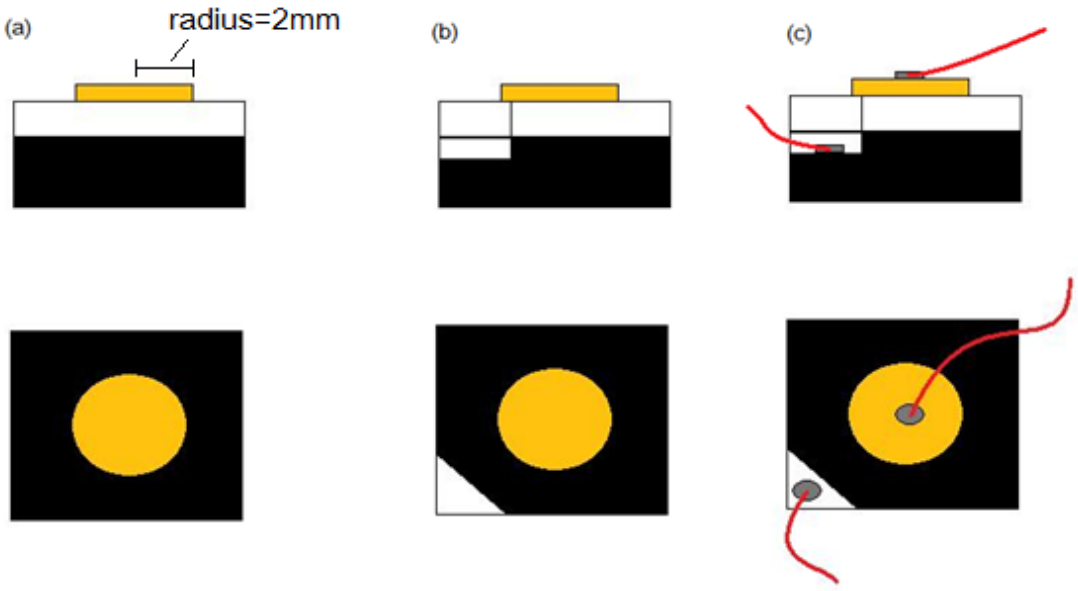

Fig. 3.7 The patterned gold film prepared by evaporative deposition is about 60 nm-thick and the radius is 2 mm. The yellow region is gold, the black is NSTO substrate, the transparent is o-$LuMnO_3$ thin film and the red lines are copper wires connecting the electrode with the gray silver paste.

Then we set the sample on the stage expander module and connected the wires to the pin of the stage. There is a circuit stretching out of the expander module for connecting to various instruments (like LCR meter or precision premier II).

Chapter 4 Results and Discussion

4.1 The structural and the magnetic properties of target

4.1.1 The structural property of target

The hexagonal $LuMnO_3$ (h-$LuMnO_3$) bulk prepared by solid-state reaction method was used as target for PLD to deposit orthorhombic $LuMnO_3$ (o-$LuMnO_3$) thin films. As shown in Fig. 4.1, the X-ray diffraction (XRD) pattern of h-$LuMnO_3$ powder was consistent with the pattern obtained from the JCPDS database for h-$LuMnO_3$. (cf. Fig. 4.2)

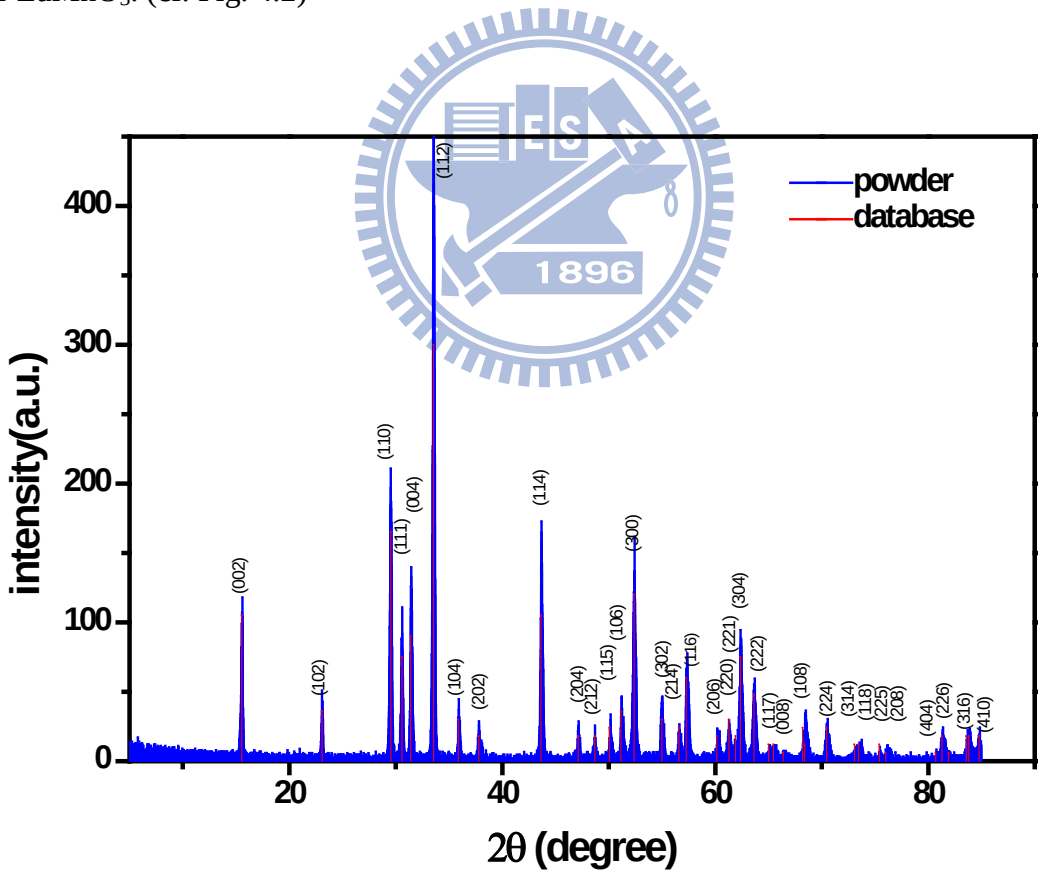

Fig.4.1 The XRD patterns of h-$LuMnO_3$ powder.

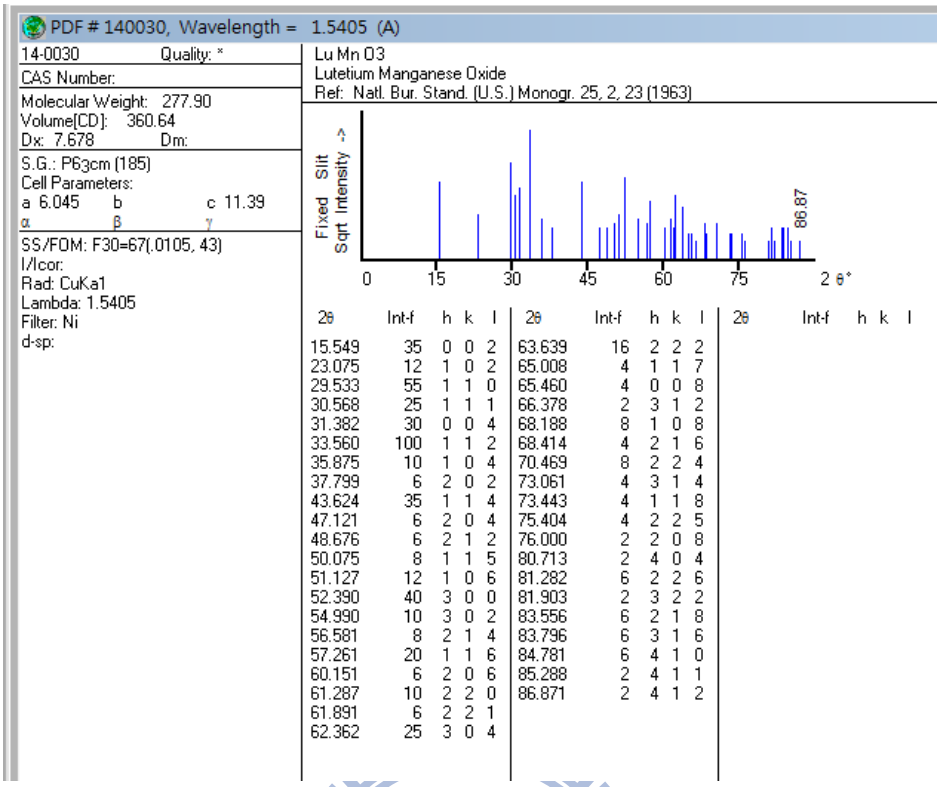

Fig.4.2 The XRD pattern of h-$LuMnO_3$ from database.

4.1.2 The magnetic property of target

Temperature dependent susceptibility χ(T) of the powder of h-$LuMnO_3$ is shown as Fig. 4.3. The Neel temperature, observed at 89K is consistent with previous results [29][30][32], indicating that the target material we obtained was indeed the stoichiometric hexagonal phase $LuMnO_3$.

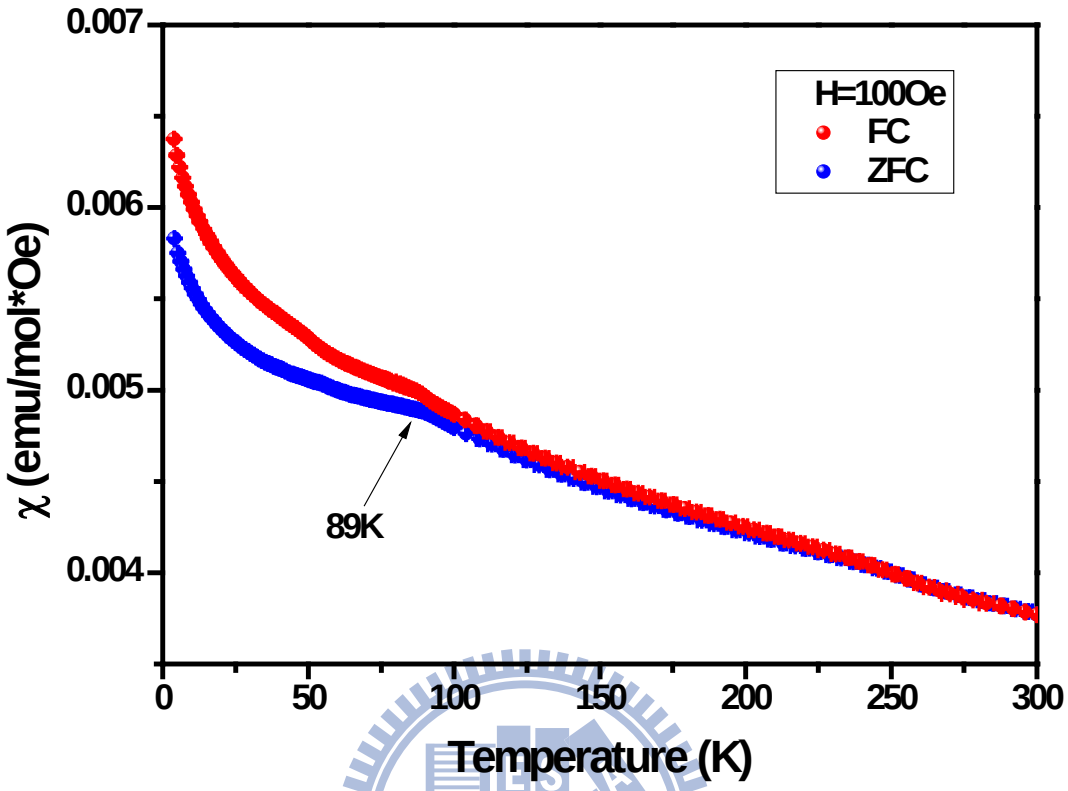

Fig.4.3 Temperature dependent susceptibility of h-$LuMnO_3$.

4.2 The characterization of o-$LuMnO_3$ thin film

4.2.1 The structural properties

The orthorhombic structure of $LuMnO_3$ can be stabilized by the epitaxial strain between film and substrate during PLD process. To find the deposition conditions for the a-axis-oriented thin film of o-$LuMnO_3$, the film were grown by using KrF excimer laser with laser energy 350mJ, repetition rate varying from 5Hz to 10Hz, substrate temperature changing from 800℃ to 880℃, and oxygen pressure ranging between 0.1 torr to 0.05 torr. Fig. 4.4 shows the XRD θ-2θ patterns of one of the o-$LuMnO_3$ thin films obtained with the conditions listed in Table 4.1. It is evident that the film is a

pure orthorhombic phase $LuMnO_3$ with clear a-axis-oriented characteristics.

Substrate	substrate temperature	oxygen partial pressure	laser energy	repetition rate
STO(110) doped Nb 0.5%wt	880℃	0.06torr	350mJ	10Hz

Table 4.1 The deposition condition of o-$LuMnO_3$ thin film.

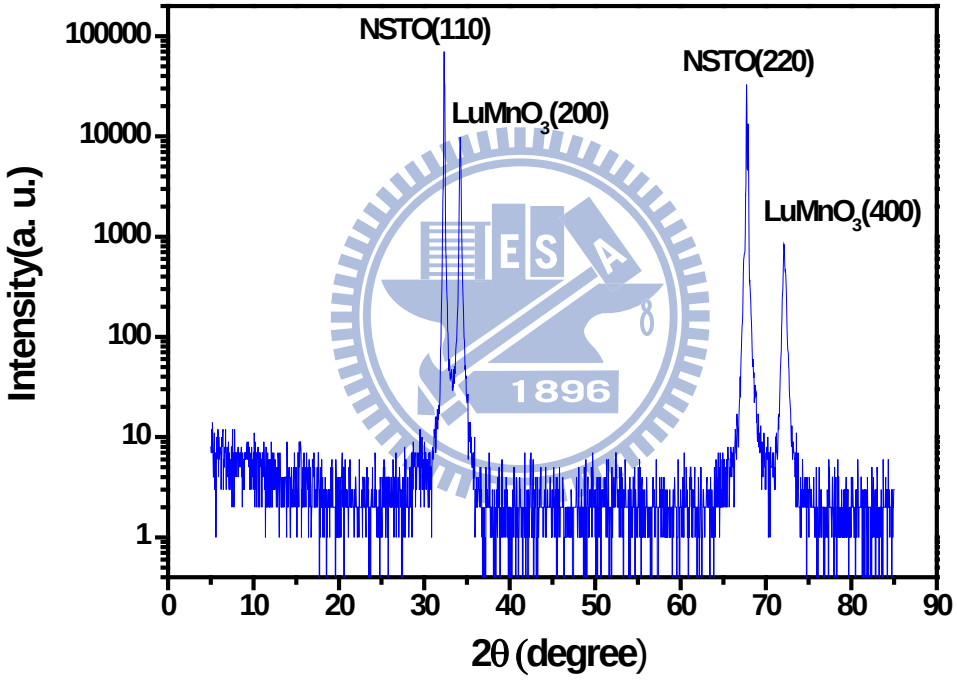

Fig.4.4 The XRD pattern of o-$LuMnO_3$/NSTO thin film.

In order to confirm the orientation-specific characteristics of the obtained films, we have further performed the Φ-scan measurements. The Φ-scan results displayed in Fig. 4.4 evidently indicate the 2-fold symmetric character of the in-plane symmetry of the film with the o-$LuMnO_3$ (220) peak and NSTO (200) peak both appearing around

180° and 360°. That means the a-axis-oriented o-$LuMnO_3$ thin film also has b axis and c axis separated and aligned along NSTO[$1\bar{1}0$] and [001], respectively (as depicted in Fig. 4.6).

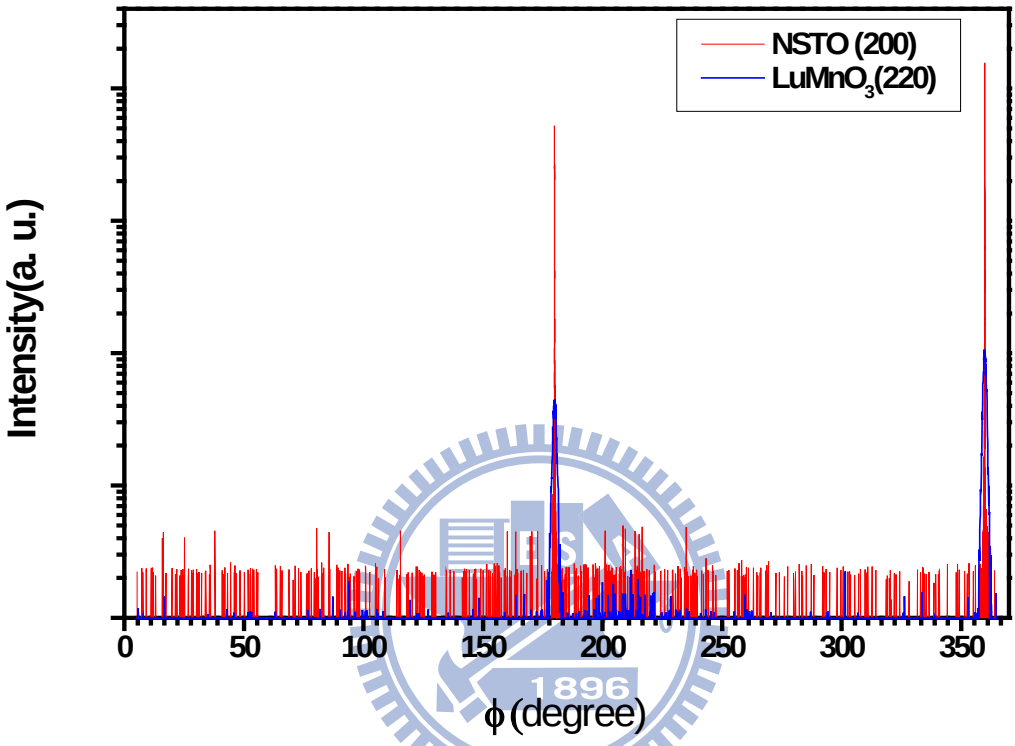

Fig.4.5 The Φ scan of the o-$LuMnO_3$/NSTO(110) thin film.

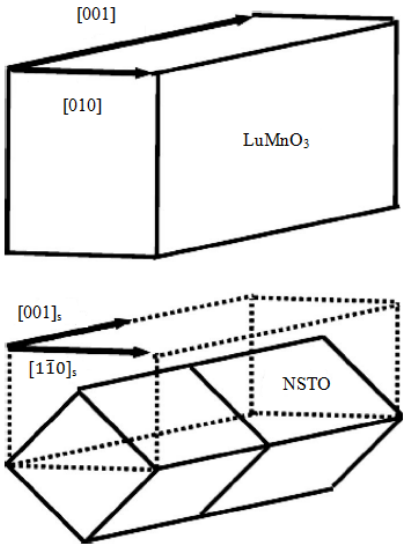

Fig. 4.6 In-plane arrangements between the o-$LuMnO_3$ thin film and NSTO (110) substrate (reproduced from reference [31]).

We have also derived the lattice constants of o-$LuMnO_3$ thin film by using the results obtained from the four-circle diffratometer. Comparing to the lattice constants reported for the bulk o-$LuMnO_3$ material [22], the obtained lattice constants for the present o-$LuMnO_3$/NSTO(110) films evidently indicate an in-plane compression along the b-axis, an in-plane stretch along the c-axis and the out-of-plane stretch along the a-axis (as shown in Table 4.2), respectively.

Table 4.2 The fitting parameters and in-plane mismatch between o-$LuMnO_3$ thin film and substrate were listed as follows:

	a axis (Å)	**b axis (Å)**	**c axis (Å)**	**V (Å^3)**
database[22]	**5.199**	**5.789**	**7.297**	**219.618**
o-$LuMnO_3$ on NSTO(110)	**5.231**	**5.675**	**7.468**	**221.700**
NSTO(110) substrate		**5.523**	**7.810**	
in-plane mismatch with substrate		**-4.83%**	**6.57%**	
strain factor	**0.61%**	**-1.96%**	**2.34%**	**0.95%**

The thickness of thin films is about 100 nm as derived from the periodicity of Kiessig fringe from X-ray reflectometry measurement, which is consistent with that obtained from α-step measurements (XRR pattern as shown in Fig. 4.7). This result is consistent with the measurement of alpha step.

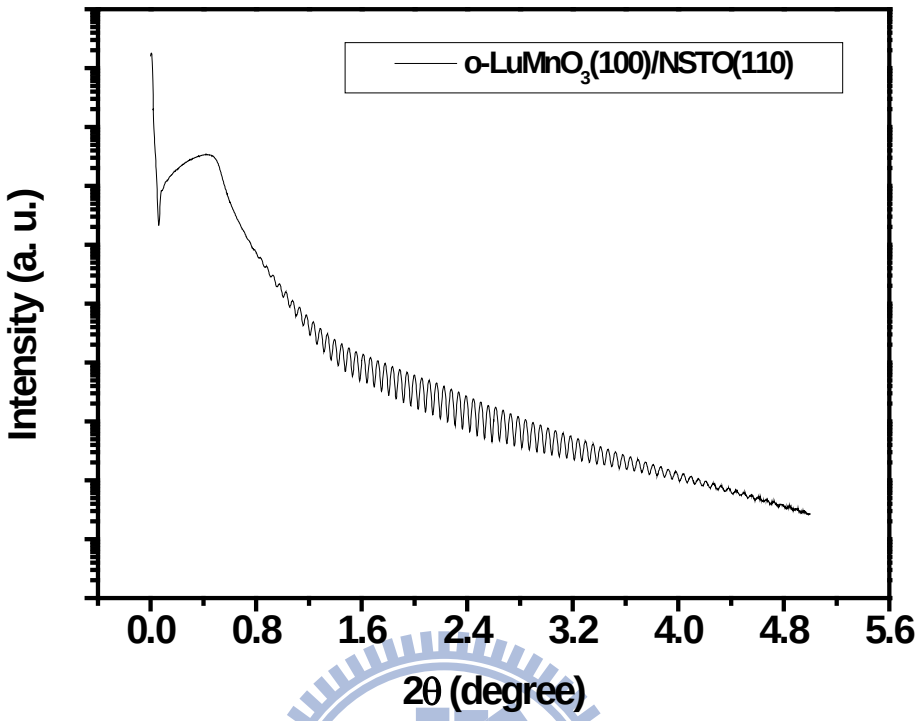

Fig. 4.7 The X-ray reflectometry (XRR) pattern of o-$LuMnO_3$ thin film.

4.2.2 The magnetic properties

Fig. 4.8 shows the temperature dependent susceptibility χ(T) of the o-$LuMnO_3$/NSTO(110) measured by field cooling (FC) and zero field cooling (ZFC) schemes with an external magnetic field of 1000 Oe (H=1000 Oe) applied along the three respective crystallographic orientations. As shown in figure, all ZFC χ(T) curves of the o-$LuMnO_3$ display an antiferromagnetic transition of Mn moment near 43K, which is consistent with previous result [12].

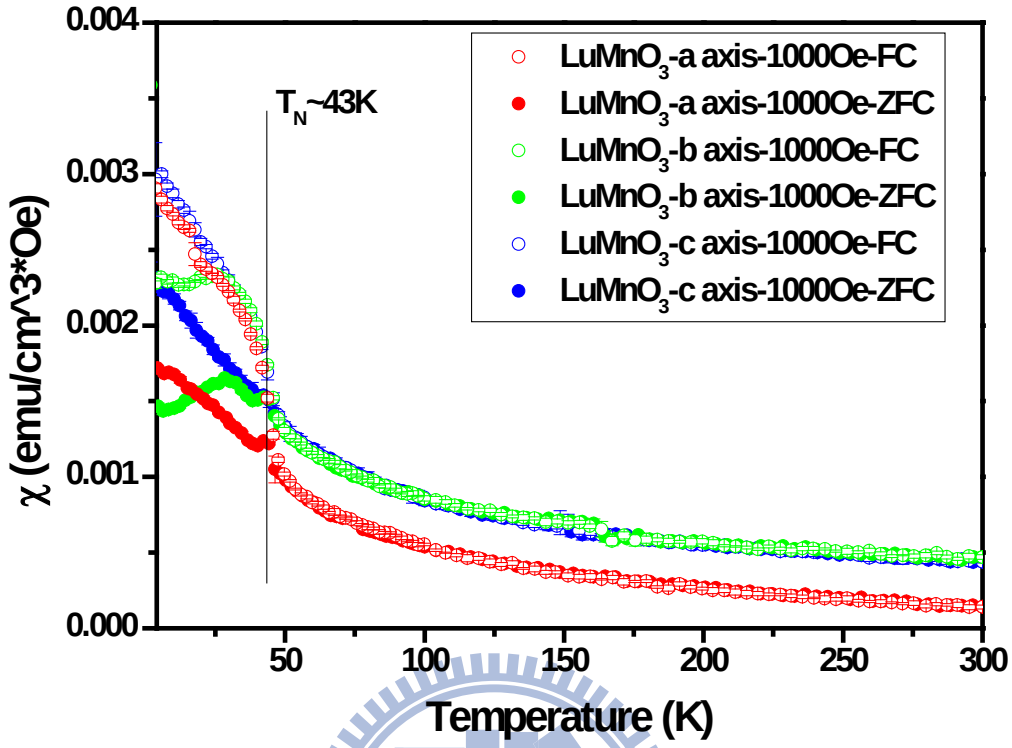

Fig. 4.8 The temperature dependent susceptibility of o-$LuMnO_3$/NSTO(110) with external field applied along the three principal crystallographic orientations.

The second magnetic transition appearing around 30K was observed exclusively in b-axis. As shown in Fig. 4.9 and Fig. 4.10, this transition is quite robust and appears to be unchanged with the external magnetic field of 1000 Oe and 500 Oe, respectively. The transition may be due to the spin reordering (T_{SR}) of Mn magnetic moment because the electric configuration of Lu^{3+} ion is [Xe] $4f^{14}$ that means Lu^{3+} ion has zero magnetic moment and has no contribution to magnetization. Along the a- and c-axis, however, there is no discernible transition observed with the same applied external field (1000 Oe or 500 Oe), as shown in Fig 4.11.

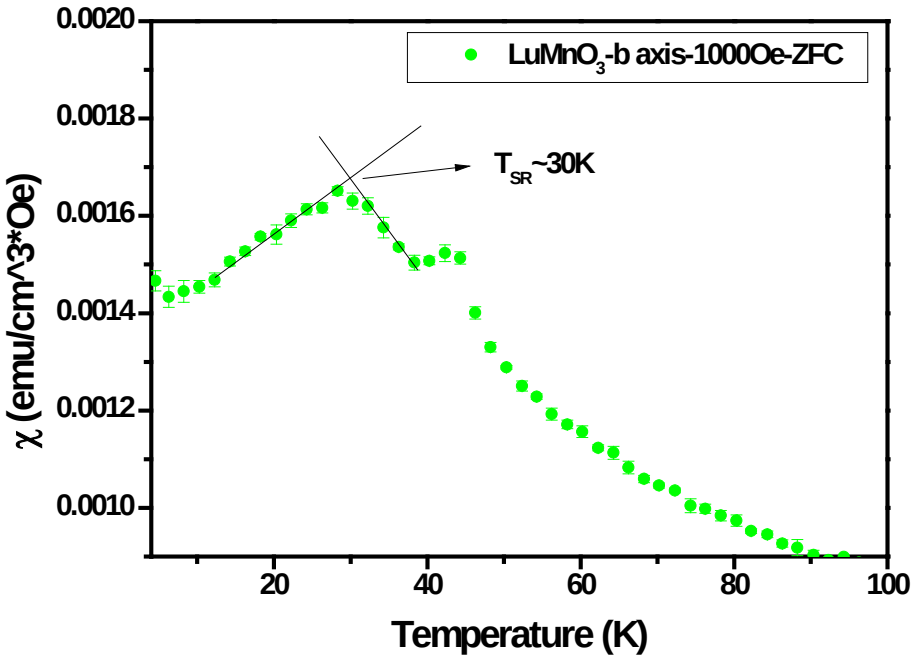

Fig. 4.9 The spin reordering (T_{SR}) of Mn moment is around 30K with the external field of 1000 Oe.

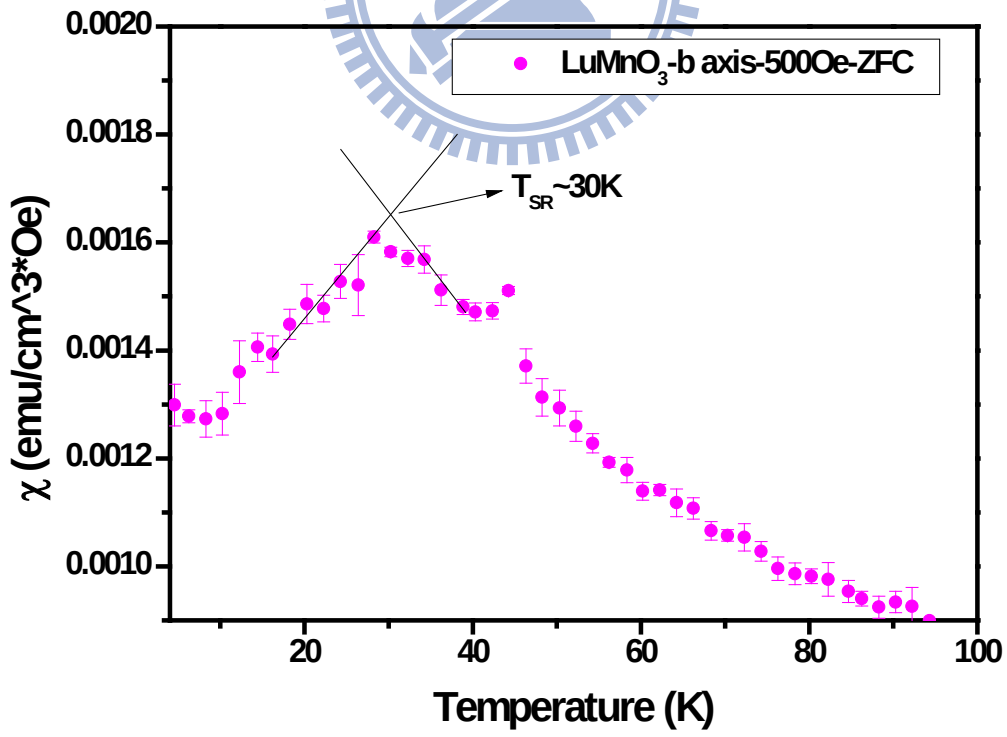

Fig. 4.10 The spin reordering (T_{SR}) of Mn moment is around 30K with the external field of 500 Oe.

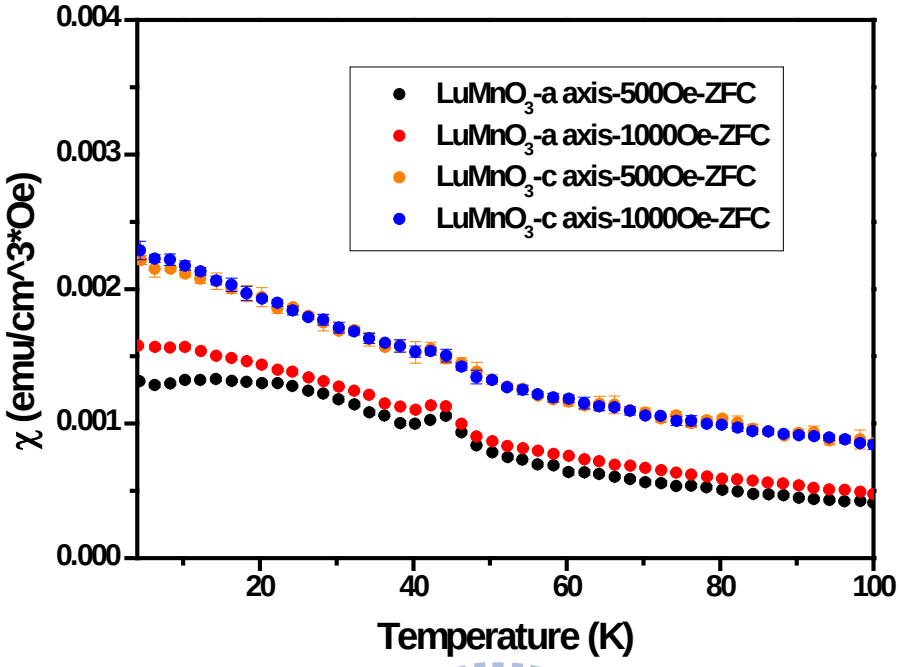

Fig. 4.11 χ(T) curves of the a- and c-axis orientation with H=500 Oe and 1000 Oe.

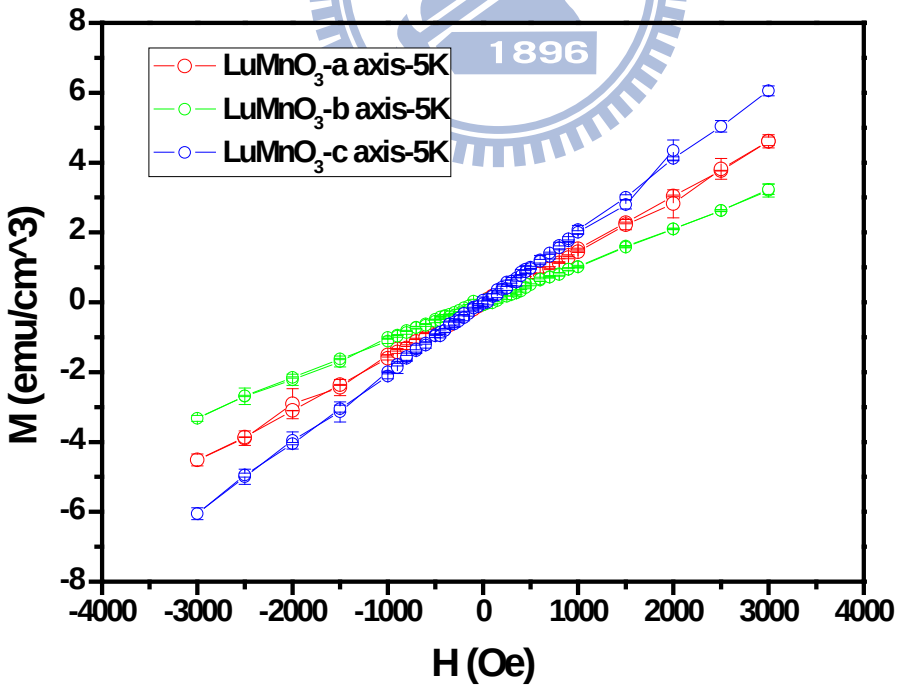

Fig. 4.12 The magnetic field dependent magnetization for o-$LuMnO_3$/NSTO(110)

at 5K with H//a(red line), H//b(green line) and H//c(blue line), respectively.

To further elaborate the nature of the observed low temperature magnetic transition, the dependence of the magnetization on magnetic field taken at 5 K for $LuMnO_3$/NSTO(110) is shown in Fig. 4.12. The linear behavior observed along the three principal crystallographic orientations suggests that the system remains with a antiferromagnetic ordered structure, similar to that seen in o-$LuMnO_3$ polycrystals [22].

4.2.3 The magnetic structure of o-$LuMnO_3$

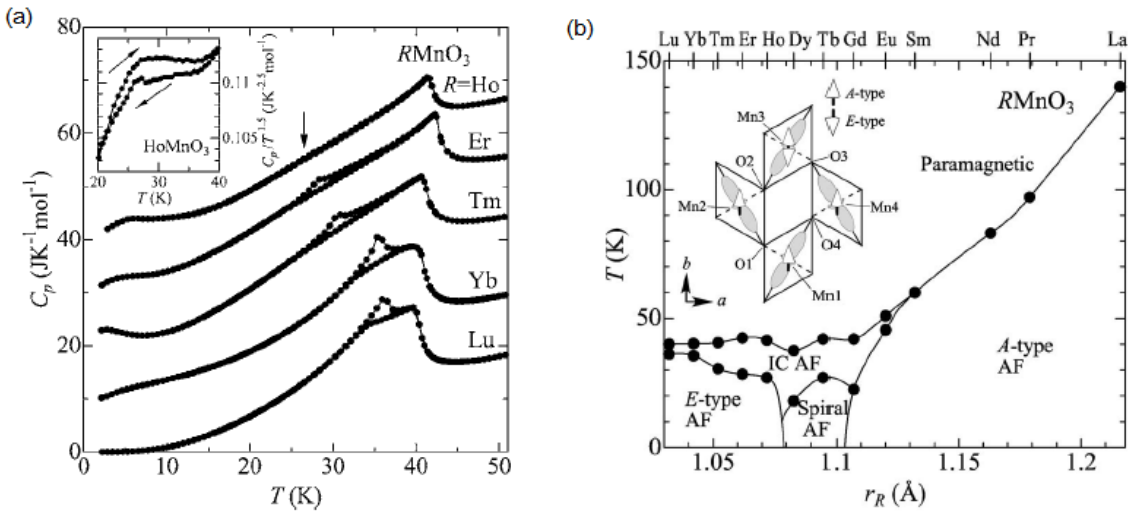

Fig. 4.13 (a) The heat capacity of $RMnO_3$, (b) Magnetic phase diagram for $RMnO_3$ as a function of the ionic radius of R(r_R) [23].

In Fig. 4.13(a), there were two transitions in heat capacity measurements for the o-$LuMnO_3$ polycrystals and one was assigned to be T_N~40K while the other was identified to be T_{lock} (illustration as Fig. 4.13(b)) [23]. Okamoto et al. [22] have reported, by performing the neutron powder diffraction at 8K, that the magnetic

ordering of the o-$LuMnO_3$ polycrystals is the E-type antiferromagnetic phase. They also reported that the Neel temperature is about 40K as observed by magnetic susceptibility measurement. No T_{lock} was reported, however, in [22].

In contrast, the magnetic properties of the o-$LuMnO_3$ (100) thin films grown on NSTO (110) substrate exhibited an apparent Néel temperature with T_N~43K regardless of the crystallographic axis probed, while the spin reordering (T_{SR}~30K) was found only in b-axis. As has been suggested previously [4, 13, 28], the influence of strain on Mn-O-Mn bonds presumably may affect the magnetic properties of the material. Considering the significant strain existing in the strain-stabilized o-$LuMnO_3$ films, similar effects are expected and may be the primary reason for the phenomena observed here.

4.2.4 The electric properties

In any case, it is our primary motivation to see if there is any correlation between the magnetic transition and the associated electric polarization. In this regard, we show in Fig. 4.14 the temperature-dependent relative permittivity $\varepsilon_r(T)$ of o-$LuMnO_3$(100) thin film measured by applying 1 kHz ac signal with amplitude of 10 mV. It is evident from Fig. 4.13, there exists a relative permittivity anomaly around 30K.

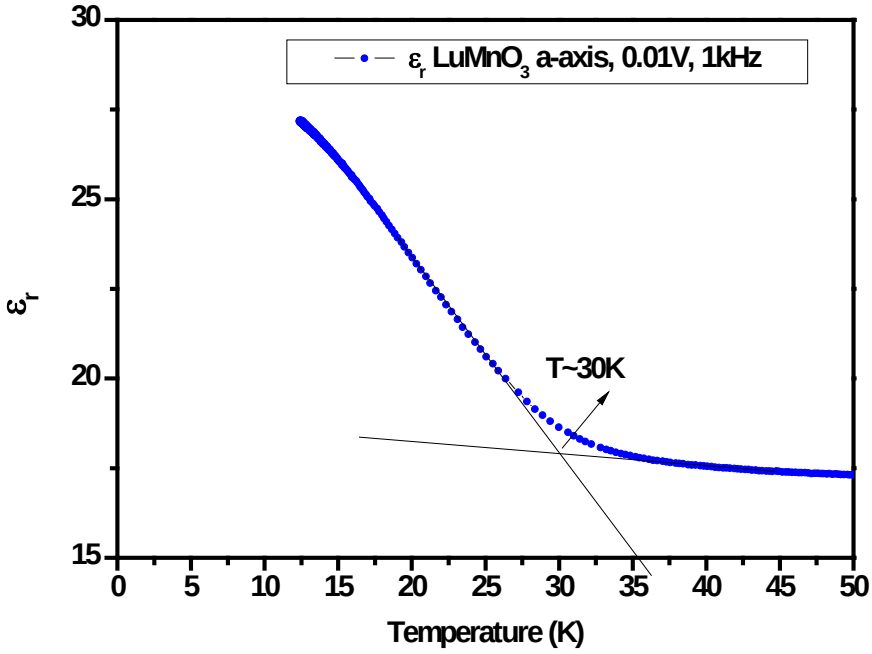

Fig. 4.14 The temperature dependent relative permittivity of o-$LuMnO_3$ thin film (E//a).

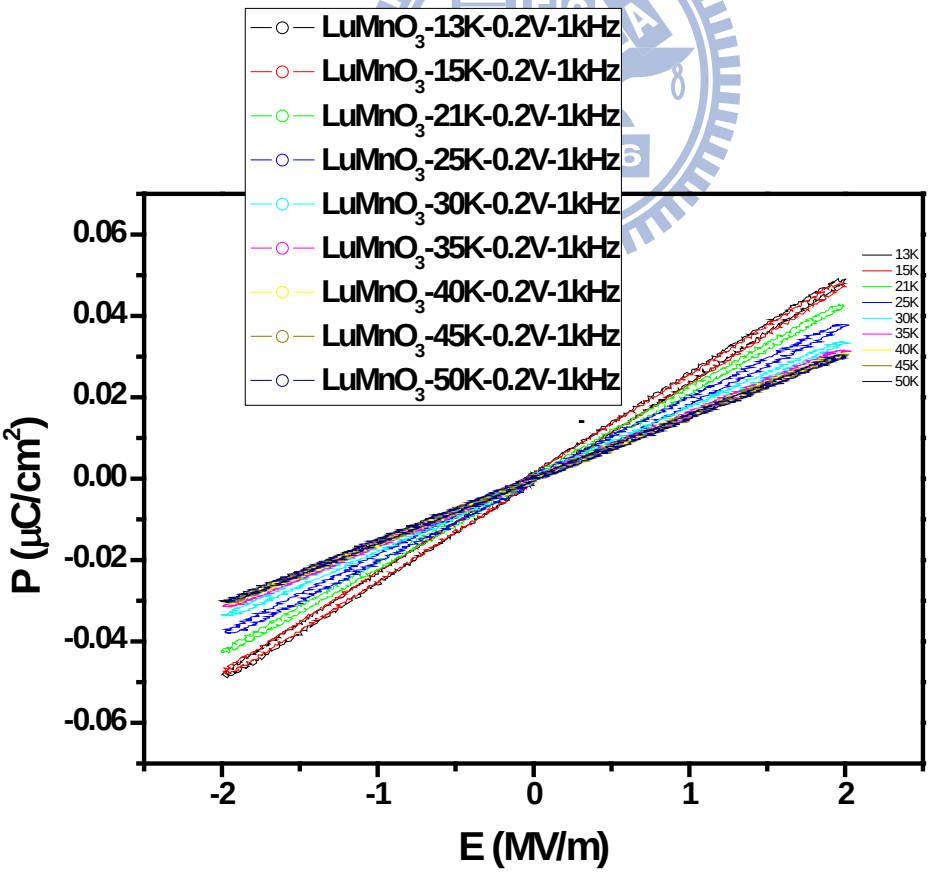

Fig. 4.15 The electric field dependent polarization with E//a at different fixed temperature for o-$LuMnO_3$/NSTO(110).

However, as shown in Fig. 4.15, the electric field dependent polarization measured at different temperatures (ranging from 13K to 50K) does not show any hysteresis loops as expected for typical ferroelectric materials. Instead, even with the measuring temperatures varied over the range of T_{SR} and T_N, the behavior of P-E curves is still linear. The separation looks like hysteresis, which was caused by the conductivity of the thin film. The absence of the spontaneous polarization suggests that the relative permittivity anomaly probably was not a direct consequence of a ferroelectric transition.

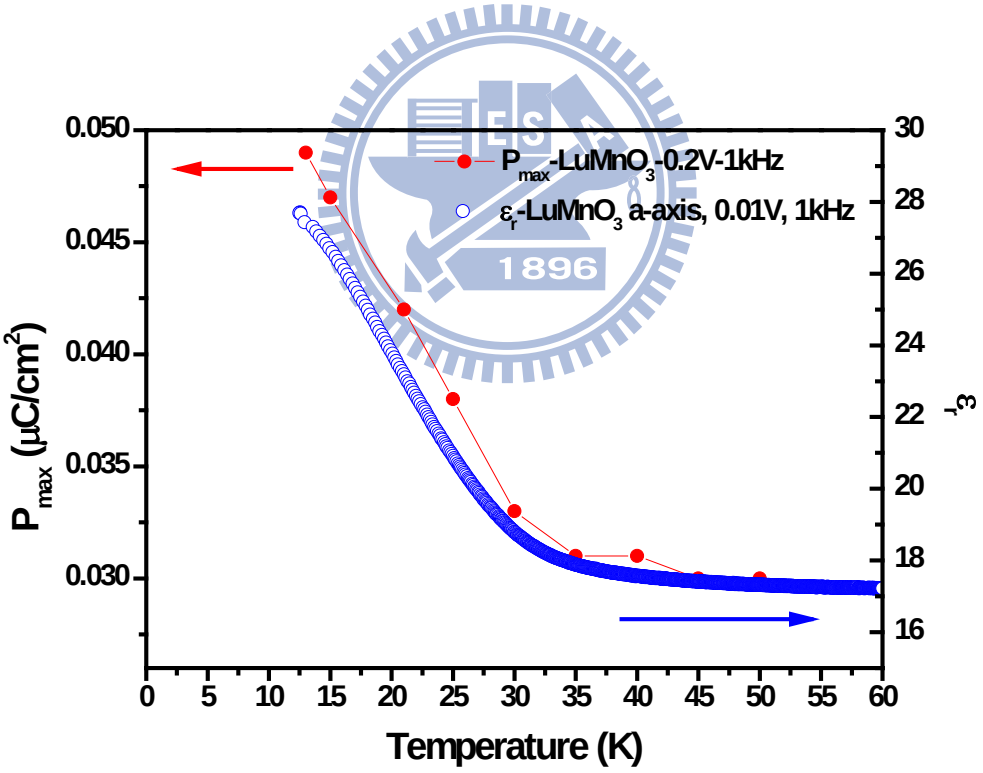

Fig. 4.16 P_{max} from Fig. 4.15 compares with the relative permittivity in Fig. 4.14.

We compared the maximum of polarization in Fig. 4.15 at different fixed temperature with the temperature dependent relative permittivity. The tendency is

consistent to each other. The slope of P-E curves may be related to the relative permittivity by the following expressions:

$$P = \frac{Q}{A} = \frac{CV}{A} = \frac{1}{A}\frac{\varepsilon_o \varepsilon_r A}{d} Ed = \varepsilon_o \varepsilon_r E$$

Where P is polarization, Q is the electric quantity calculated by the instrument, A is the area of the thin film, V is the applied voltage, C is the capacitance of the thin film, d is the thickness of the thin film, E is the electric field, ε_r is relative permittivity and ε_0 is vacuum permittivity. The slope of P-E curves derived from Fig. 4.14 matches the relative permittivity shown in Fig. 4.13 very well.

4.3 Measurement of standard samples

For the check of our circuit, we used standard samples, which were provided by Radiant Technologies, to make sure of the ferroelectric hysteresis loop measurement of our system. The linear capacitance (1.004 nF) and the ferroelectric capacitance (PZT) are connected to our circuit and tested individually. The P-E curves are shown as the Fig. 4.17 and Fig. 4.18.

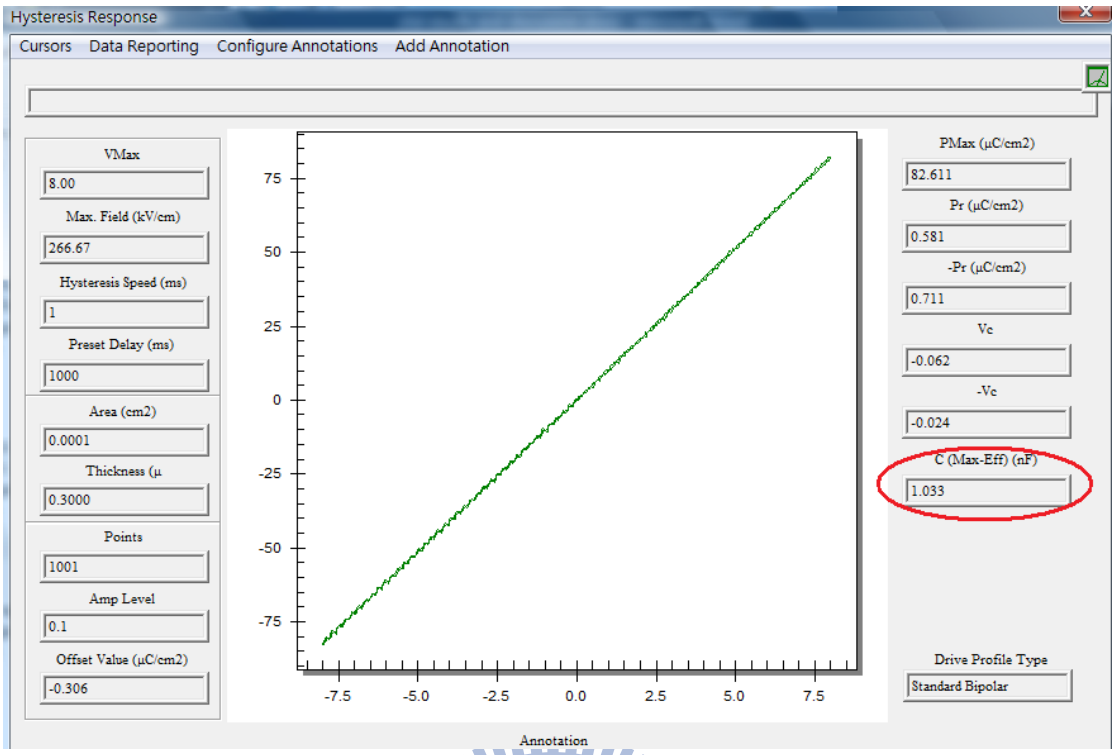

Fig. 4.17 The result of linear capacitance test shows that the circuit is accuracy in capacitance test.

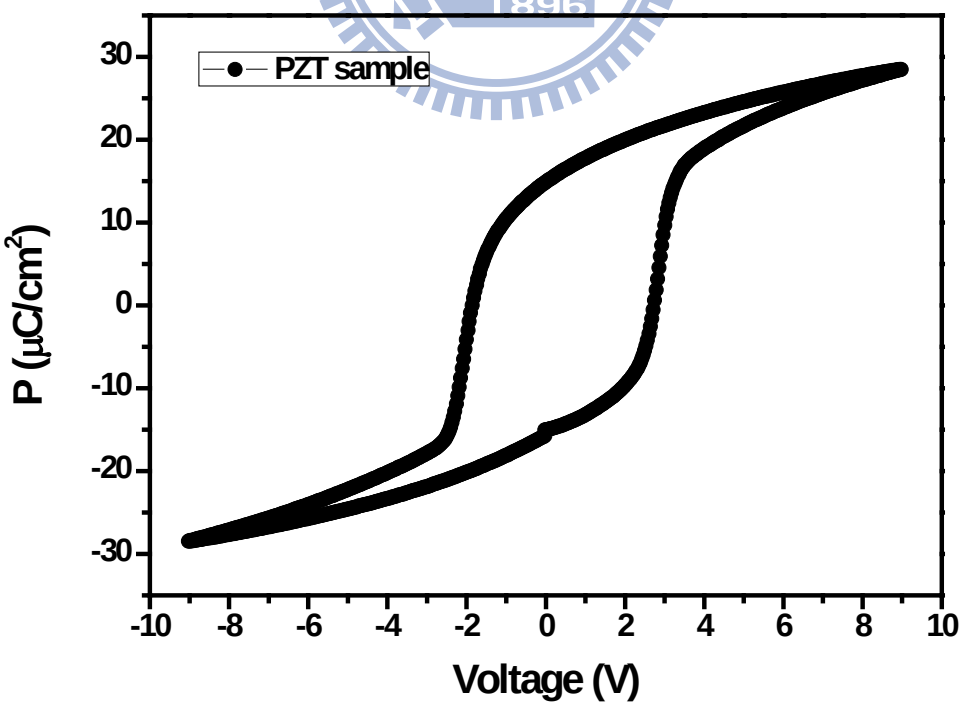

Fig. 4.18 The P-E curve shows that the system can measure the ferroelectric hysteresis character.

4.4 The correlation between strain, electric, and magnetic properties

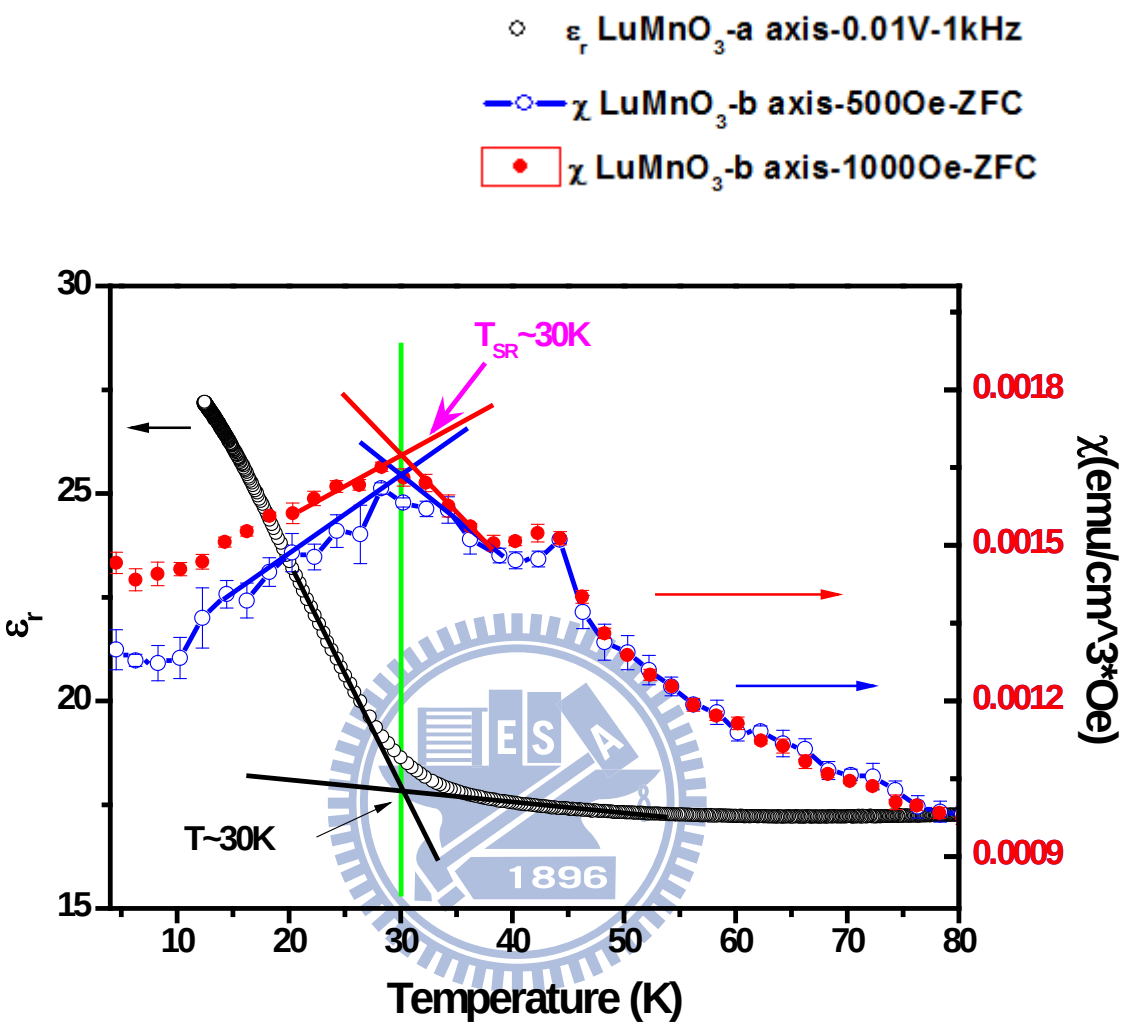

Fig. 4.19 The plot shows the χ(T) curves with applied magnetic field(H=500 Oe and 1000 Oe) along b-axis, and the ε_r(T) curve by applying 1 kHz ac signal with amplitude of 10 mV (E//a).

Finally, we compare the results of χ(T) and ε_r(T). As shown in Fig. 4.19, the anomaly seen in ε_r(T) around 30K coincides with the second magnetic transition T_{SR}. Thus, it is quite natural to correlate the observed ε_r(T) anomaly with the magnetism-induced ferroelectric transition as suggested theoretically by Sergienko et

al. [5]. The missing of the expected P-E hysteresis is not understood at present. However, we note that the strain effect of o-$LuMnO_3$ thin film was not considered in the theory and the strain effect has been demonstrated to cause changes in the magnetic properties [4, 13, 28].

The epitaxial strain plays the essential roles, which are stabilizing the structure of o-$LuMnO_3$ and affecting the magnetic properties. Considering the lattice distortion, the crystal elastic energy is promoted to the higher level. Assume the elastic energy is the $E \propto x^2$, which x is the displacement of ions, as shown in Fig. 4.20.

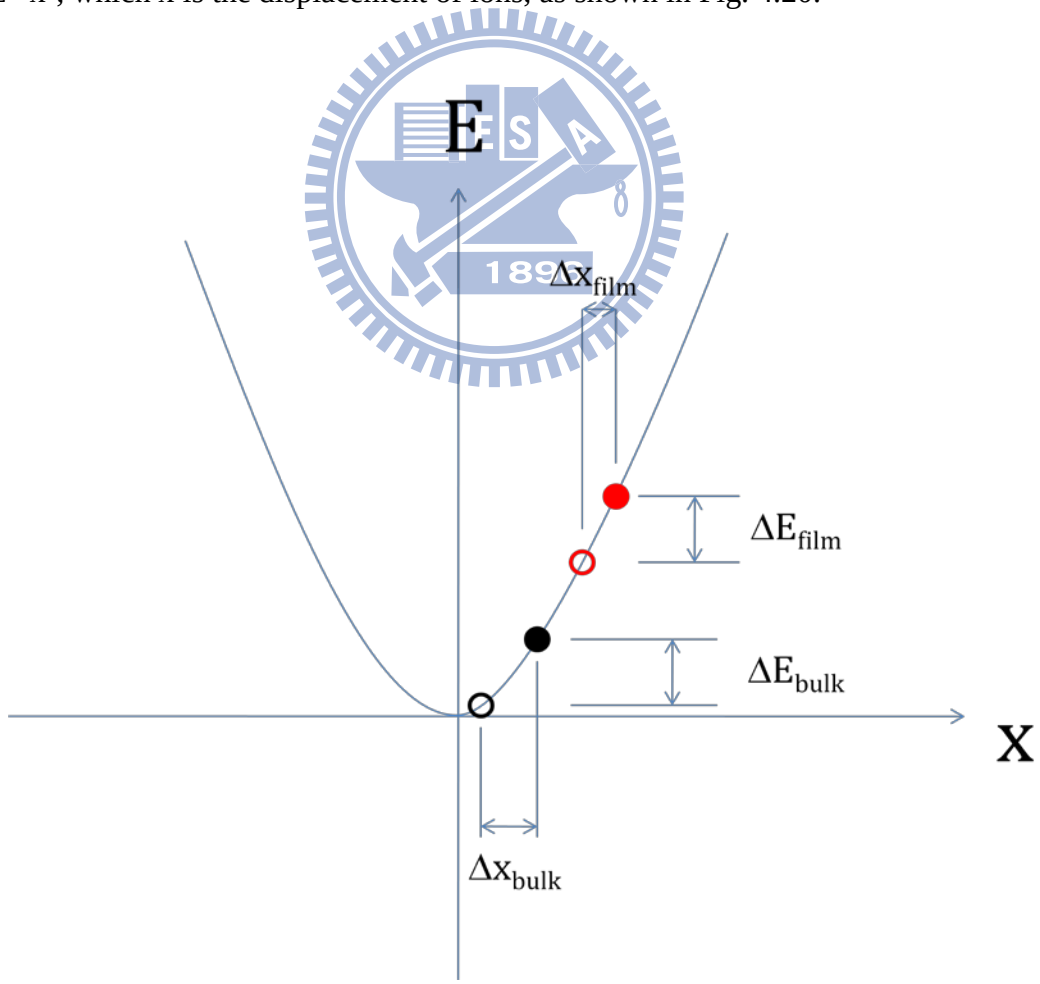

Fig. 4.20 The schematic illustration of relation between the ion displacement and the elastic energy.

The red hollow circle is the state of the o-$LuMnO_3$ thin film with no distortion caused by double exchange. The red full circle is the state considered double exchange. And the black is the o-$LuMnO_3$ bulk, respectively. The bulk preparation is using the process of high temperature and high pressure, which may cause a little strain, so the black hollow circle is not at zero of x. The thin film is distortion by the epitaxial stress of substrate compared with the bulk, which is more strain than the bulk. Supposing the same hopping energy in the bulk and the thin film, the displacement is much different. The distortion of the thin film is rather small than that of the bulk, which may reduce the polarization very much, even totally.

Somehow it may also affect the correlation of magnetoelectric properties. In any case, further studies are certainly needed in order to clarify the discrepancies described above.

Chapter 5 Summary

The a-axis oriented o-$LuMnO_3$ films were successfully grown on NSTO (110) by PLD. X-ray diffraction and Φ-scan allowed us to confirm the structure of $LuMnO_3$ was orthorhombic with specific growth directions. Using SQUID to measure the anisotropic magnetization, an antiferromagnetic transition of Mn moment were observed near 43K in each axis and the second transition (T_{SR}) was observed around 30K only in b-axis. Furthermore, we probed the polarization and the relative permittivity with electric field applied along a-axis. The linear behavior of P-E curves at fixed temperature (T ranged from 13K to 50K) indicates the absence of spontaneous polarization. The temperature dependent relative permittivity revealed the anomaly around 30K may have correlation with the second magnetic transition (T_{SR}) in b-axis. The difference between the experiment and theoretic prediction is presumably due to the strain effect, but need further investigations to clarify.

Reference

[1] S. W. Cheong and M. Mostovoy, Nature Mater. **6**, 13 (2007).

[2] T. Kimura, T. Goto, H. Shintani, K. Ishizaka, T. Arima, and Y. Tokura, Nature **426**, 55 (2003).

[3] M. Gajek, M. Bibes, S. Fusil, K. Bouzehouane, J. Fontcuberta, A. Barthelemy, and A. Fert, Nature Mater. **6**, 296 (2007).

[4] T. H. Lin, H. C. Shih, C. C. Hsieh, C. W. Luo, J. Y. Lin, J. L. Her, H. D. Yang, C. H. Hsu, K. H. Wu, T. M. Uen, and J. Y. Juang, J. Phys.: Condens. Matter **21**, 026013 (2009).

[5] I. A. Sergienko, C. Sen, and E. Dagotto, Phys. Rev. Lett. **97**, 227204 (2006).

[6] S. Picozzi, K. Yamauchi, B. Sanya, I. A. Sergienko, and E. Dagotto, Phys. Rev. Lett. **99**, 227201 (2007).

[7] K. Yamauchi, F. Freimuth, S. Blügel, and S. Picozzi, Phys. Rev. B **78**, 014403 (2008).

[8] S. Picozzi, K. Yamauchi, I. A. Sergienko, C. Sen, B. Sanyal, and E. Dagotto, J. Phys.: Condens. Matter **20**, 434208 (2008).

[9] C. Y. Ren, Phys. Rev. B **79**, 125113 (2009).

[10] S. Ishiwata, Y. Kaneko, Y. Tokunaga, Y. Taguchi, T. H. Arima, and Y. Tokura, Phys. Rev. B **81**, 100411 (2010).

[11] X. Martí, V. Skumryev, V. Laukhin, F. Sánchez, M.V. García-Cuenca, C. Ferrater, M. Varela, and J. Fontcuberta, J. Mater. Res. **22**, 2096 (2007).

[12] T. Y. Tsai, *Anisotropic magnetic properties of orthorhombic $LuMnO_3$ thin films*, A master thesis submitted to NCTU, R.O.C. (2009).

[13] C. C. Hsieh, *Magnetic and electronic characteristics of substrate-stabilized hexagonal and orthorhombic multiferroic rare earth manganite thin film*, A

Dissertation Submitted to NCTU, R.O.C. (2008).

[14] R. L. Comstock., *Introduction to magnetism and magnetic recording*, (1999).

[15] C. Zener, Phys. Rev. **82**, 403 (1951).

[16] P. W. Anderson and H. Hasegawa, Phys. Rev. **100**, 675 (1955).

[17] Y. Tokura and N. Nagaosa, Science **288**, 462 (2000).

[18] B. N. Figgis and M. A. Hitchman, *Ligand Field Theory and Its Applications*, (2000).

[19] H. A. Jahn and E. Teller, Proc. Roy. Soc. A. **161**, 220 (1937).

[20] W. Prellier, M. P. Singh and P. Murugavel, J. Phys.: Condens. Matter **17**, R803 (2005).

[21] T. Imai, M. Sasaura, K. Nakamura and K. Fujiura, NTT Tech. Rev. ,**5** 9 (2007).

[22] H. Okamoto, N. Imamura, B. C. Hauback, M. Karppinen, H. Yamauchi, and H. Fjellvag, Solid State Commun. **146**, 152 (2008).

[23] M. Tachibana, T. Shimoyama, H. Kawaji, T. Atake, and E. Takayama-Muromachi, Phys. Rev. B **75**, 144425 (2007).

[24] T. Goto, T. Kimura, G. Lawes, A. P. Ramirez, and Y. Tokura, Phys. Rev. Lett. **92**, 257201 (2004).

[25] T. Kimura, S. Ishihara, H. Shintani, T. Arima, K. T. Takahashi, K. Ishizaka, and Y. Tokura, Phys. Rev. B **68**, 060403 (2003).

[26] M. Kenzelmann, A. B. Harris, S. Jonas, C. Broholm, J. Schefer, S. B. Kim, C. L. Zhang, S. W. Cheong, O. P. Vajk, and J.W. Lynn, Phys. Rev. Lett. **95**, 087206 (2005).

[27] M. Mostovoy, Nature Mater. **7**, 269 (2008).

[28] K. T. Chang, *Structure and magnetic properties in orthorhombic $ErMnO_3$ thin film*, A master thesis submitted to NCTU, R.O.C. (2009).

[29] D. G. Tomuta, S. Ramakrishnan, G. J. Nieuwenhuys, and J. A. Mydosh, J. Phys.: Condens. Matter **13**, 4543 (2001).

[30] K. Yoshii and H. Abe, J. Solid State Chem. **165**, 131 (2002).

[31] T. C. Han and J. G. Lin, Appl. Phys. Lett. **94**, 082502 (2009).

[32] K. Uusi-Esko, J. Malm, N. Imamura, H. Yamauchi, and M. Karppinen, Mater. Chem. Phys. **112**, 1029 (2008).